Afar triple junction fed by single asymmetric mantle upwelling

Emma J. Watts[1*], Rhiannon Rees[1], Thomas M. Gernon[1], Philip Jonathan[2,3], Derek Keir[1,4], Rex N. Taylor[1], Melanie Siegburg[5], Emma L. Chambers[6], Carolina Pagli[7], Matthew J. Cooper[1], Agnes Michalik[1], J. Andrew Milton[1], Thea K. Hincks[1], Ermias F. Gebru[8,9], Atalay Ayele[9]

[1]School of Ocean and Earth Science, University of Southampton, National Oceanography Centre, European Way, Southampton, SO14 3ZH, UK

[2] Department of Mathematics and Statistics, Lancaster University, Lancaster, UK

[3]Shell Research Limited, London, UK

[4] Dipartimento di Scienze della Terra, Università degli Studi di Firenze, Firenze 50121, Italy

[5] Landesamt für Geologie und Bergwesen Sachsen-Anhalt, Halle (Saale), Germany

[6] School of Cosmic Physics, Geophysics Section, Dublin Institute for Advanced Studies, Dublin, Ireland

[7] Dipartimento di Scienze della Terra, Università di Pisa, Pisa 56126, Italy

[8]Department of Geosciences, University of Fribourg, Fribourg, Switzerland

[9]School of Earth Sciences, Addis Ababa University, Addis Ababa, Ethiopia

*Corresponding Author Email: e.watts@soton.ac.uk

Mantle upwellings drive large-scale surface volcanism and facilitate continental breakup and ocean basin formation [1-3]. However, the spatial characteristics and internal constitution of these upwellings as they impact the tectonic plate are poorly resolved. The Afar Triangle, East Africa, is widely considered to be underlain by a deep-sourced and broad-scale mantle hotspot or plume [4, 5], although the existence of such a plume has been hotly contested [6]. This region, a classic triple junction comprising three rifts at various stages of evolution, allows us to examine the controls—including those related to

tectonics—on the behaviour and distribution of upwelling mantle. Here, we present extensive new geochemical data spanning the triple junction to show that the mantle beneath Afar comprises a single, asymmetric upwelling. Using statistical modelling to integrate our new geochemical data with existing geophysical constraints, we identify a spatially and chemically heterogeneous upwelling [7, 8, 9], and find that it fundamentally controls the composition and abundance of melt in all three rift arms. We identify variations in mantle compositions on characteristic length scales of about 50 to 200 km, which are higher in the more advanced and faster-extending rift arms, suggesting more rapid channelised mantle flow. Our findings demonstrate the susceptibility of mantle upwellings to the dynamics of overriding plates.

Introduction

Mantle plumes or hotspots, that is, upwellings of the mantle that originate between depths of 1,000 and 2,800 km [10], are anomalously hot zones of the mantle and/or zones of an enriched composition which reduce the solidus temperature, favouring partial melting [10]. The role of such upwellings in driving volcanism during continental breakup has long been debated (e.g. [11, 12]). However, our understanding of rift-upwelling interactions remains incomplete with only a small fraction of Earth's upwellings situated under continents [13] and a limited number of upwellings associated with active continental rifting [14]. In the 'classic' magma assisted continental rift, the Afar triple junction—where the Arabian, Nubian, and Somalian tectonic plates intersect—all three rifts are currently volcanically and tectonically active [15], making it an ideal location to study the interactions between mantle upwelling and continental rifting. Here, the driver of melt production is debated with some models suggesting decompression melting with minimal upwelling involvement [6], while others propose the upwelling of hot, deep mantle [16], or even multiple upwellings [17, 18]. Whilst several discrete segments of the rift have been studied in terms of magma petrogenesis (e.g., [16, 19]), a paucity of high-precision geochemical data has hampered our ability to comprehensively evaluate the spatial characteristics of upwelling across the broader region and thereby rigorously test existing models. To overcome this limitation, we begin our study by implementing a comprehensive sampling strategy, targeting young volcanoes spanning all three rift systems (Main Ethiopian Rift [MER], Red Sea Rift and the Gulf of Aden Rift) (Fig. 1).

Probing the presence of a mantle upwelling

We analyse rocks that are Quaternary in age (i.e., less than 2.58 million years (Myr) old), and from volcanoes that have been active during the Holocene period, which began 11.7 thousand years ago (ka) [20]. By targeting younger rocks, we aim to make a direct comparison with geophysical data across the region, enabling an integrated exploration of mantle petrogenesis and dynamics.

Our new compilation includes over 130 rock samples, approximately doubling the number of high-quality analyses in the area, with many of these from previously unstudied volcanoes. These samples were carefully selected from a repository covering the broader Afar region (see Methods for details), supplemented by additional samples collected during fieldwork in the MER. To examine spatial trends in the geochemistry of surface volcanism, all samples were analysed for major and trace elements alongside radiogenic isotopes (Sr, Nd, Pb; see Methods). We also integrate high-quality data from the open-source GEOROC data repository (https://georoc.eu/ [25]) for rocks, including the classic catalogue from [18] (i.e., the Gulf of Aden), where a complete set of analyses is available within the area of interest. Additionally, we leverage recent spatial maps of key geophysical variables, such as the depth of the Mohorovičić Discontinuity [26] (see Methods) and shear wave velocities at regularly spaced depths (i.e., 40, 60, 80, 100, and 120 km [27]). These variables provide wellestablished proxies for the boundary between the crust and mantle, as well as for the presence and abundance of melt within the lithosphere and asthenosphere [27]. Collectively, this information allows us to infer details about the depth, extent, and compositional characteristics of melts distributed across all three rifts.

Mantle upwellings, commonly associated with reduced seismic velocities (Vs, Vp) [28, 29], are widely accepted to tap a deep-mantle component called C (common [30]) and/or FOZO (i.e., focus zone [31]). Such components typically exhibit an isotopically distinct composition (that is, generally low $^{87}Sr/^{86}Sr$, high $^{143}Nd/^{144}Nd$, and high $^{206}Pb/^{204}Pb$ [31]) and elevated trace element ratios ($\Delta Nb > 0$, see Eq. A1 [32]; $Ce/Pb > 30$). We find that all samples within our study region, specifically, within 500 km of the Afar triple junction, exhibit strong C/FOZO signatures (Fig. 1 and Extended Data Fig. 1), supporting a first-order deep upwelling control on the composition and abundance of melt [18, 29, 30]. When we apply a spline interpolation to the data (see Methods), we detect prominent isotopic and geochemical variations across the broader region (Fig. 1). This includes distinctly elevated La/Sm, Ce/Pb, and $^{206}Pb/^{204}Pb$, and decreased $^{87}Sr/^{86}Sr$ and shear wave speeds in northern Afar, central Afar (near the triple junction), and sporadically along the MER and Gulf of Aden Rift (Fig. 1 and Extended Data Fig. 1). These spatial trends implicate an underlying complexity to magmatism and mantle upwelling, which has previously been inferred using geochemical (e.g., [33]) and geophysical approaches (e.g., [23, 26, 27, 34]).

These data and observations enable us to test multiple models of mantle upwelling dynamics. The first model we consider is a simple, homogeneous mantle upwelling impinging at the triple junction (e.g., [18]), which is expected to produce a systematic shift in variables traditionally taken to indicate deep upwelling radially with distance (Fig. 2). Extending this model, we then allow the upwelling to be spatially and temporally heterogeneous, as reported in the Hawaiian [35] and Canary Island [9] volcanoes. This mechanism yields a similar pattern to the first model centred at the triple junction but accommodates compositional fluctuations over the radial distance corresponding to the arrival of chemically distinct pulses (Fig. 2).

We additionally test whether the spatial variations observed (Fig. 1 and Extended Data Fig. 1) are best explained through the presence of numerous small-scale upwellings, which have been proposed based on geophysics and numerical models (e.g. [23], Fig. 2). Using the data summarised in hexmaps (Fig. 1 and Extended Data Fig. 1), we test this model using three upwellings: one centred on the triple junction, one on the Red Sea Rift north of the Afar region, and one in the southern MER, with the positions of these loci informed by previous observations (see Methods). The strong mantle signatures observed across the wider area (Fig. 1 and Extended Data Fig. 1b) suggest that crustal assimilation has played a relatively minor role in recent magmatism. This inference is consistent with geochemical and isotope evidence, which indicate that crustal assimilation had a more significant impact on the composition of magmatism during earlier stages of rifting, at approximately 30 Ma, when the continental crust was thicker and magmatic fluxes were higher [36]. In contrast, the current crust is thinned and has been intruded by mafic melts along the length of the rift axes. Seismicity analysis indicates that recent magmatic activity beneath the rift axis in Afar is transient [37] and, in turn, that magmas are unlikely to reside in crustal reservoirs for long enough to extensively assimilate crustal lithologies.

To interrogate this further, we explore the correlation between key geochemical and geophysical indicators (Fig. 3b) and the depth to the Moho (boundary between crust and mantle used to indicate crustal thickness), as crustal thickness is widely thought to influence the degree of assimilation [36] (Methods). We found that most indicators, including Pb isotopes—a reliable indicator of crustal assimilation [38]—exhibit only a weak, but significant, correlation with the Moho depth (Fig. 3b). On the other hand, Ce/Pb exhibits a strong negative correlation (i.e., Pearson correlation coefficient of -0.7), indicating that where the crust is thin, the Ce/Pb values are high, and vice versa. This trend can be attributed to minimal crustal assimilation across most of the region, but increasing as the crust thickens within the MER. Nevertheless, we test the crustal assimilation influence further by excluding cases where Ce/Pb values fall below 20 and which could feasibly be associated with crustal assimilation [36, 38].

Afar Mantle Upwelling's Spatial Characteristics

To test between a singular upwelling (hereafter, model 'C1C', Fig 2) and small-scale upwellings (model 'C3C', Fig 2), we identify 14 key geochemical and geophysical variables (for descriptions, see Extended Table 2) and calculate the distance, using the spherical cosine law (see Methods), between the purported upwelling centre [5, 18, 24] and each observation site (Methods). We then apply two-deep cross validation to find the optimum linear fit (that is, representing a homogeneous upwelling) and penalised B-spline fit (that is, representing a heterogeneous upwelling) to each of the variables over a radial distance of 500 km—the radial limit of data points considered within this study (Fig. 3c and Extended Data Fig. 2). The predictive performance of each fit is then assessed by calculating the mean standardised root-mean squared error of prediction (RMSEP; Fig. 3a), where a value of 1 indicates a lack of predictive capability, and 0 a perfect predictive ability. For both initial models (C3C and C1C) we observe the B-spline fit (i.e., a class of polynomial functions) to have the best predictive performance, compared to a linear fit (Fig. 3a). This indicates that a compositionally heterogeneous upwelling is most likely (Figs. 3a and 3c). However, minimal differences in predictive performance are observed between the single upwelling model (C1C 'heterogeneous' spline; RMSEP = 0.76) versus the small-scale upwelling model (C3C 'heterogeneous' spline; RMSEP = 0.75), assuming the distribution with distance is symmetrical across all rifts.

It is plausible that variable extension rates between the three rift systems [15] introduces further complexity to the geochemical and geophysical signals. Accordingly, we introduce three further models, C1D, C3D, and C3X (Figs. 2 and 3a; see Methods) to investigate how regional factors may influence upwelling behaviour. Models C1D and C3D consider one upwelling and three small-scale upwellings respectively, while allowing for distinct distance-dependent patterns for each rift, thereby modelling the distribution of the indicators across each rift independently. Unlike the other models, C3X allows each small-scale upwelling to have a distinct signature, as well as permitting an independent distribution along each rift (Methods). We then obtain the optimum linear and B-spline fit for these three models. This analysis indicates that the overall best predictive model is the B-spline fit of C1D, wherein a single, heterogeneous mantle upwelling is present, albeit with differing distributions of key variables (Extended Data Table 2) between rift-arms. This model yields a mean standardised RMSEP of 0.59 (Fig. 3a). Whilst the Red Sea Rift and MER have a high sample density, the Gulf of Aden is lacking due to limited sample availability. However, when excluding the Gulf of Aden rift from our analyses, the overall trend between the models remains the same (Extended Data Fig. 5b). Using additional analysis, we confirm that excluding cases in which Ce/Pb < 20 does not affect our overall results (Extended Data Fig. 5a), suggesting that primary mantle variations exert the first-order control on magma compositions. While the rifts share a common compositionally heterogenous upwelling, they appear to behave independently, implying that some feature of their tectonic regime modulates the observed signals.

Interplay Between Upwelling and Segmentation

We find that many of the optimum splines for each rift display distance-dependent sinusoidal patterns (Fig. 3c and Extended Data Fig. 2). Importantly, our analysis indicates that the variability observed for some indicators within the MER are of greater amplitude and shorter periodicity with distance compared to those of the Red Sea Rift (Fig. 3c and Extended Data Fig. 2). Further, the observed variation in Pb isotopes within the Red Sea Rift suggests that the upwelling may be chemically heterogeneous across some elements, but more uniform in others (i.e., $^{87}Sr/^{86}Sr$ and $^{143}Nd/^{144}Nd$). Although ΔNb values are broadly consistent across the region, we identify small-scale differences in La/Sm and Vs velocity at 100 km depth (within the likely melt-rich zone in the asthenosphere [39]) with distance in each rift (Fig. 3c and Extended Data Fig. 2). This feature likely indicates locally variable degrees of melting across the region, which in turn raises the question: do the zones of locally higher melt fraction and variable isotopic compositions observed in one rift correspond to those observed in the other rifts, thus potentially indicating a shared melt source?

To address this question, we carried out principal component analysis (PCA) and K-mean cluster analysis using all variables post-standardisation (see Methods). Across all variables, the K-means cluster analysis algorithm seeks to group similar observations whilst minimising the within-cluster total sum of squares for a pre-specified number of clusters. Our results from K-means cluster analysis (Extended Data Fig. 4; Methods), show a higher number of clusters, smaller in geographic size, assigned to the MER (50-100 km length scale, 4 clusters) compared to the Red Sea Rift (150-200 km length scale, 3 clusters). Several clusters are found to co-exist in different rift-arms (clusters 1-3). For example, samples assigned to cluster 3 are observed in the distal section of Red Sea Rift, as well as in locations closer to the rift centre within the MER (Extended Data Fig. 4). The three clusters (1-3) observed across the Red Sea Rift match the initial ~200 km clustering sequence observed across the MER. This compositional similarity may indicate that they are derived from the same parent melt, although the distribution of these melts within the MER appears to be more condensed over shorter distances compared to the Red Sea Rift.

The spatial distribution of these clusters reflects variations in the composition and abundance of melt (Extended Data Fig. 4) and shares some cursory similarities to the magmatic segments observed at the surface (Extended Data Fig. 4). However, when inspected in detail we observe clear differences. For example, volcanic systems both within magmatic segments and the adjacent rift flanks are commonly allocated to single clusters, and the boundaries between clusters and known magmatic segments are typically mismatched (Extended Data Fig. 4). In Afar, the length scale of clusters is longer than that of magmatic segments. We therefore infer that the compositional variability is unlikely to be related to the along-axis segmentation of crustal subvolcanic plumbing systems.

Instead, we appeal to a deeper process. Taken together, our data can be explained through a single upwelling model with internal heterogeneity that varies between rifts (e.g., [9]), as shown by the spline model. Crucially, the K-means cluster analysis indicates the heterogeneity in the rifts repeat, pointing toward a geochemically pulsing upwelling as observed for other mantle plumes (e.g., [9]). Rifts act as natural channels that are exploited by upwelling melt from deeper mantle sources [40]. Considering the high extension rate in Afar (10.5-19.5 mm/yr; [21]) compared to that of the MER (~ 5.2 mm/yr; [21]), it is plausible that a mantle flow rate is impeded by the narrowing of the rift between Afar and the MER. This process would lead to a 'bottleneck' effect [40, 41, 42], like that associated with the Galapagos plume [43]. This may in turn result in a different length-scale of mantle heterogeneity (Fig. 3; Extended Data Fig. 2) between the rifts (Extended Data Fig. 4). Further, a contrast in crustal thickness is evident between the rifts, with the MER crust being thicker (25-33 km [44]) compared to that of Afar (16-25 km [45]; Extended Data Fig. 1). Assuming a correlation between crustal and overall plate thickness, this effect would likely introduce differences in mantle flow rate along each rift. A progressive thickening of the overlying lithosphere away from the upwelling centre in the MER should reduce the volume capacity for melt, impeding the mantle flow. Consequently, the heterogeneous nature of the pulsing upwelling would likely exhibit a more condensed pattern within the MER compared to Afar, as we observe (Extended Data Fig. 4).

We conclude that variations in melt composition and abundance within Afar is best explained by a heterogeneous pulsing mantle upwelling that is not symmetrical (Extended Data Fig. 4), but instead shaped by varying extension rates within each rift (Fig. 4). Whilst this model principally investigates the likelihood of a singular or three-small-scale upwelling scenario, our results demonstrate that for either option, a heterogeneous upwelling provides the best match to multiple observations in the region. The observed variations in melt composition and abundance between the MER and Afar imply that the length scale of heterogeneities within magma-assisted rifting environments may be controlled not only by the upwelling itself, but by the rift extension rate and plate thickness. If this model is correct, it carries important implications for understanding the dynamical evolution of magmatism within continental rifts undergoing the rift-to-drift cycle.

Acknowledgements

E.J.W was supported by Natural Environmental Research Council UK through the INSPIRE Doctoral Training Partnership [grant number NE/L002531/1] and Wyley Fund of the Geologists' Association. We acknowledge the use of rocks from the Afar Repository of the University of Pisa, Italy (http://repositories.dst.unipi.it/index.php/home-afar). We appreciate all those directly or indirectly involved in the field-campaign in the 1960s and acknowledge their contributions to the growing research within the region. We thank G.L. Foster and M. Cassidy for their helpful comments on the manuscript.

Author Contributions

E.J.W. conceived the idea, processed the data, and prepared the manuscript. T.M.G and D.K. advised on the work and assisted with sampling and interpretation. P.J. wrote the code for the statistical modelling and assisted with interpretation. T.K.H advised on the statistical analysis. E.J.W., R.R., M.S., M.J.C., A.M., J.A.M., and R.N.T analysed the samples and processed the geochemical data. E.L.C processed the geophysical data for the sample locations. E.J.W., T.M.G., and D.K. wrote the manuscript with input from all co-authors.

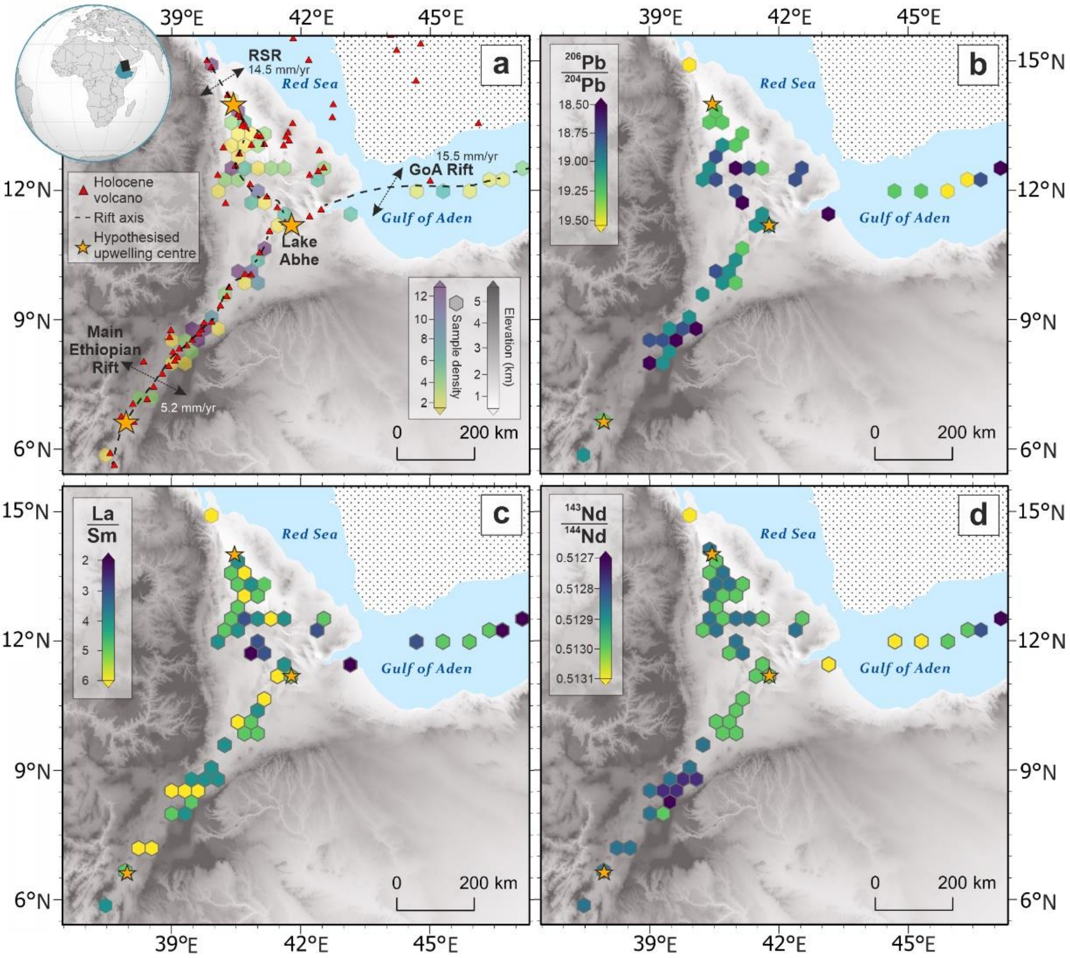

Fig. 1: Variation in geochemical and geophysical properties in the Afar Triangle; (a) Map showing the Gulf of Aden (GoA) Rift, Red Sea Rift (RSR) and the Main Ethiopian Rift (MER) rift axes shown by dashed lines and associated rifting rates indicated by arrows (after [21] & [22]). The three hypothesised [18, 23, 24] upwelling locations (yellow stars) and Holocene volcanoes (red triangles) are shown. Hexmap colours show the density of samples within the hexagons' area with purple representing >12 and yellow showing 1-2. Location of maps shown on global inset (black rectangle). (b) Hexmap showing the ^{206}Pb/^{204}Pb variations across the study region (dark blue = low upwelling signature ^{206}Pb/^{204}Pb, yellow = high ^{206}Pb/^{204}Pb). (c) Hexmap showing the La/Sm variations across the study region (yellow = high La/Sm – high melt fraction, dark blue = low La/Sm – low melt fraction). (d) Hexmap showing the ^{143}Nd/^{144}Nd variations across the study region. Yellow indicates a high upwelling-like ^{143}Nd/^{144}Nd, dark blue = low ^{143}Nd/^{144}Nd).

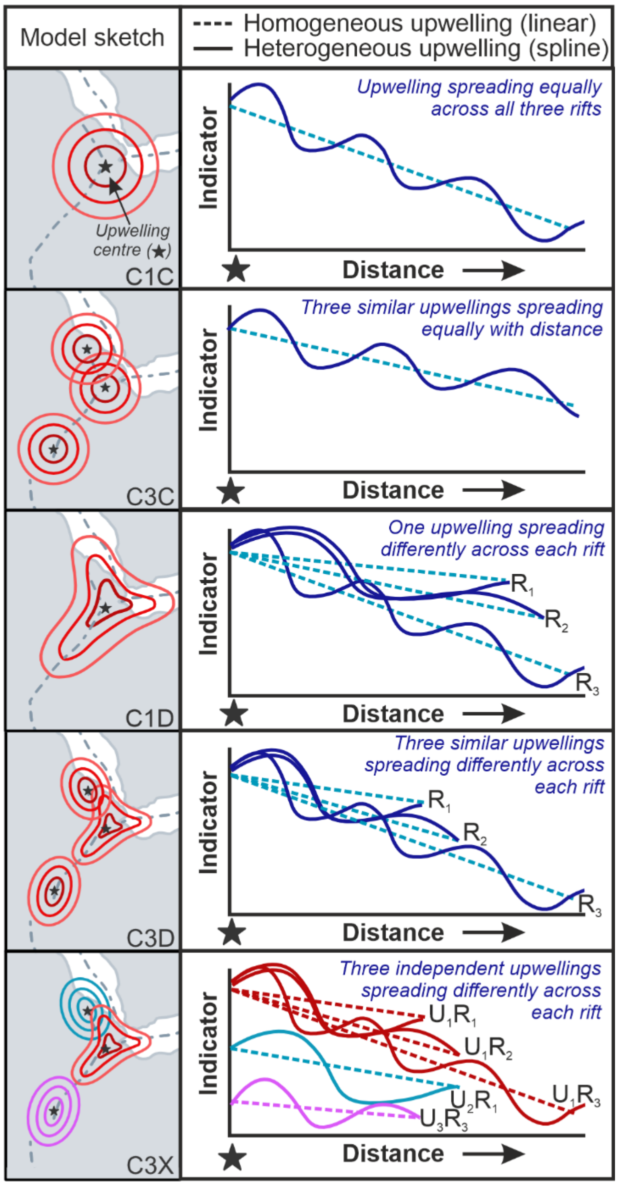

Fig. 2: Models of mantle upwellings beneath Afar tested in this study. Schematic diagram of the upwelling scenarios for Afar that were tested within this study. The diagrams (left) are labelled with the code associated with each model (see Extended Table 1 and the Statistical Analyses section within Methods for further details). The number of lines, shown on the schematic graphs (right), equals the number of models that must be fitted for that model variant (linear = dashed, spline = continuous), where R = Rift and U = upwelling. Note that each model variant has been illustrated with an indicator that decreases with a reduction in upwelling proportion. The location of the purported mantle upwellings are shown by the star symbol.

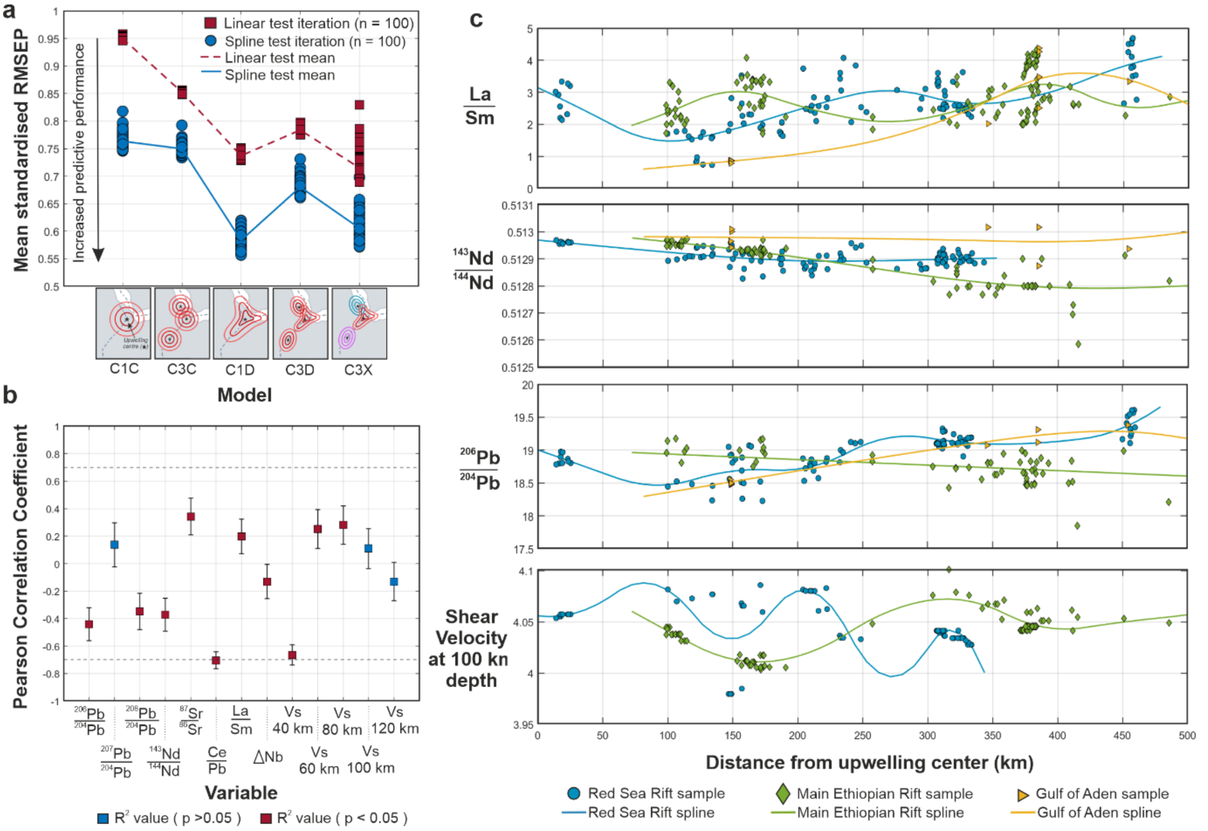

Fig. 3: Statistical analysis of Afar rift properties; (**a**) The mean standardised root means square error of prediction (RMSEP) for each of the models tested. Individual linear model results are shown by red squares and the mean of those results are displayed by the red line. Individual spline results are shown by blue circles and the mean of those results are shown by a blue line. All models were run for 100 iterations to capture the likely uncertainty distribution, as shown by the data points. (**b**) Pearson correlation coefficient of each of the selected 13 variables with Moho depth. Error bars show the 95-percentile error of the coefficient. Red squares indicate where the correlation is significant ($p < 0.05$) and blue squares indicate that the correlations are not deemed significant ($p > 0.05$). **(c)** Splines (a smooth, flexible polynomial curve) of the best overall model (C1C) for selected variables. Symbols show the data within the study (blue circles = Red Sea Rift, green diamonds = Main Ethiopian Rift, yellow triangles = Gulf of Aden Rift). 2-sd (error) for the data points is smaller than the symbols used.

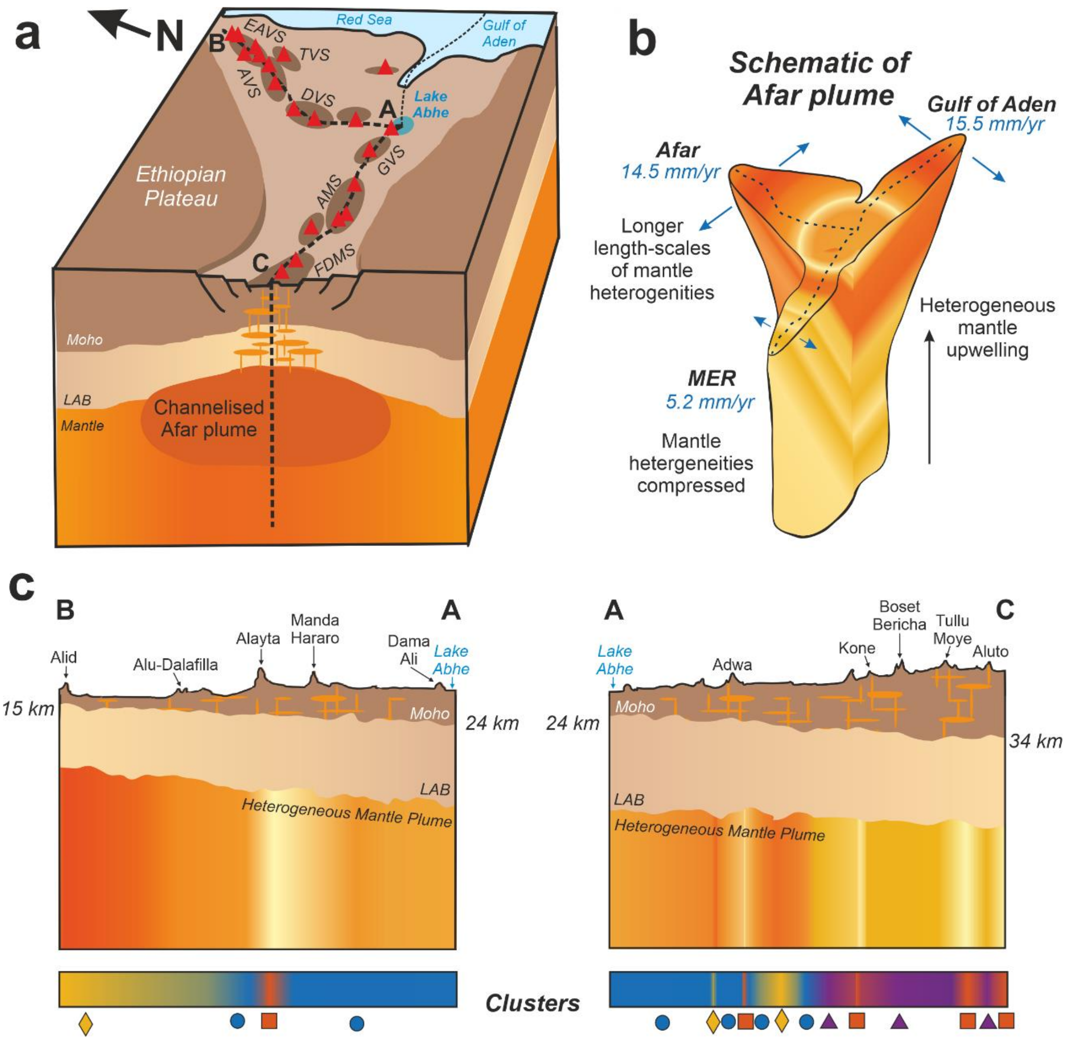

Fig. 4: Spatially heterogeneous nature of the mantle upwelling beneath Afar. (**a**) Box diagram showing the rifts across Afar and the mantle upwelling being channelised by the rift. The lines of section A-B-C are those shown in panel (**c**). Volcanic segments are shown and labelled: Erta Ale Volcanic Segment (EAVS), Tat'Ale Volcanic Segment (TAVS), Alayta Volcanic Segment (AVS), Dabbahu Volcanic Segment (DVS), Gabillema Volcanic Segment (GVS), Adda'do Magmatic Segment (AMS), Fentale-Dofen Magmatic Segment (FDMS). (**b**) Schematic of the Afar upwelling showing the dimensions of channelised flow along the three rifts (dashed lines). (**c**) Schematic cross sections along the Red Sea Rift (A-B) and MER (A-C) showing the distribution of heterogeneities within the mantle upwelling and how that maps to the clusters shown in Extended Data Fig. 4. The levels of distinct features including the Lithosphere-Asthenosphere Boundary (LAB) are not shown to scale.

References

[1] Cañón-Tapia, E., & Walker, G. P. (2004). Global aspects of volcanism: the perspectives of "plate tectonics" and "volcanic systems". Earth-Science Reviews, 66(1-2), 163-182. https://doi.org/10.1016/j.earscirev.2003.11.001

[2] Morgan, W. J. (1971). Convection plumes in the lower mantle. Nature, 230(5288), 42-43. https://doi.org/10.1038/230042a0

[3] White, R., & McKenzie, D. (1989). Magmatism at rift zones: the generation of volcanic continental margins and flood basalts. Journal of Geophysical Research: Solid Earth, 94(B6), 7685-7729. https://doi.org/10.1029/JB094IB06P07685

[4] Rooney, T. O. (2020). The Cenozoic magmatism of East Africa: part IV–the terminal stages of rifting preserved in the Northern East African Rift System. Lithos, 360, 105381. https://doi.org/10.1016/j.lithos.2020.105381

[5] Schilling, J. G. (1973). Afar mantle plume: rare earth evidence. Nature Physical Science, 242(114), 2-5. https://doi.org/10.1038/physci242002a0

[6] Rychert, C. A., Hammond, J. O., Harmon, N., Michael Kendall, J., Keir, D., Ebinger, C., ... & Stuart, G. (2012). Volcanism in the Afar Rift sustained by decompression melting with minimal plume influence. Nature Geoscience, 5(6), 406-409.https://doi.org/10.1038/ngeo1455

[7] Ito, G. (2001). Reykjanes' V'-shaped ridges originating from a pulsing and dehydrating mantle plume. Nature, 411(6838), 681-684. https://doi.org/10.1038/35079561

[8] Parkin, C. J., Lunnon, Z. C., White, R. S., Christie, P. A., & Integrated Seismic Imaging & Modelling of Margins Project (iSIMM) Team. (2007). Imaging the pulsing Iceland mantle plume through the Eocene. Geology, 35(1), 93-96. https://doi.org/10.1130/G23273A.1

[9] Taylor, R. N., Davila-Harris, P., Branney, M. J., Farley, E. R., Gernon, T. M., & Palmer, M. R. (2020). Dynamics of a chemically pulsing mantle plume. Earth and Planetary Science Letters, 537, 116182. https://doi.org/10.1016/j.epsl.2020.116182

[10] Weis, D., Harpp, K. S., Harrison, L. N., Boyet, M., Chauvel, C., Farnetani, C. G., ... & Williamson, N. M. (2023). Earth's mantle composition revealed by mantle plumes. Nature Reviews Earth & Environment, 4(9), 604-625. https://doi.org/10.1038/s43017-023-00467-0

[11] Koptev, A., Calais, E., Burov, E., Leroy, S., & Gerya, T. (2015). Dual continental rift systems generated by plume–lithosphere interaction. Nature Geoscience, 8(5), 388-392. https://doi.org/10.1038/ngeo2401

[12] Fitton, J. G. (1983). Active versus passive continental rifting: evidence from the West African rift system. Tectonophysics, 94(1-4), 473-481.https://doi.org/10.1016/0040-1951(83)90030-6

[13] Jackson, M. G., Becker, T. W., & Steinberger, B. (2021). Spatial characteristics of recycled and primordial reservoirs in the deep mantle. Geochemistry, Geophysics, Geosystems, 22(3), e2020GC009525. https://doi.org/10.1029/2020GC009525

[14] Rogers, N., Macdonald, R., Fitton, J. G., George, R., Smith, M., & Barreiro, B. (2000). Two mantle plumes beneath the East African rift system: Sr, Nd and Pb isotope evidence from Kenya Rift basalts. Earth and Planetary Science Letters, 176(3-4), 387-400. https://doi.org/10.1016/S0012-821X(00)00012-1

[15] Zwaan, F., Corti, G., Keir, D., & Sani, F. (2020). A review of tectonic models for the rifted margin of Afar: Implications for continental break-up and passive margin formation. Journal of African Earth Sciences, 164, 103649. https://doi.org/10.1016/j.jafrearsci.2019.103649

[16] Ferguson, D. J., Maclennan, J., Bastow, I. D., Pyle, D. M., Jones, S. M., Keir, D., ... & Yirgu, G. (2013). Melting during late-stage rifting in Afar is hot and deep. Nature, 499(7456), 70-73. https://doi.org/10.1038/nature12292

[17] Hansen, S. E., & Nyblade, A. A. (2013). The deep seismic structure of the Ethiopia/Afar hotspot and the African superplume. Geophysical Journal International, 194(1), 118-124. https://doi.org/10.1093/gji/ggt116

[18] Schilling, J. G., Kingsley, R. H., Hanan, B. B., & McCully, B. L. (1992). Nd-Sr-Pb isotopic variations along the Gulf of Aden: Evidence for Afar mantle plume-continental lithosphere interaction. Journal of Geophysical Research: Solid Earth, 97(B7), 10927-10966. https://doi.org/10.1029/92jb00415

[19] Hagos, M., Koeberl, C., & de Vries, B. V. W. (2016). The Quaternary volcanic rocks of the northern Afar Depression (northern Ethiopia): Perspectives on petrology, geochemistry, and tectonics. Journal of African Earth Sciences, 117, 29-47. https://doi.org/10.1016/J.JAFREARSCI.2015.11.022

[20] Smithsonian Institution: Global Volcanism Program (2013)

[21] Zwaan, F., Corti, G., Sani, F., Keir, D., Muluneh, A. A., Illsley-Kemp, F., & Papini, M. (2020). Structural analysis of the Western Afar Margin, East Africa: Evidence for multiphase rotational rifting. Tectonics, 39(7), e2019TC006043. https://doi.org/10.1029/2019TC006043

[22] Gillard, M., Leroy, S., Cannat, M., & Sloan, H. (2021). Margin-to-margin seafloor spreading in the eastern Gulf of Aden: a 16 Ma-long history of deformation and magmatism from seismic reflection, gravity and magnetic data. Frontiers in Earth Science, 9, 707721. https://doi.org/10.3389/feart.2021.707721

[23] Civiero, C., Armitage, J. J., Goes, S., & Hammond, J. O. (2019). The seismic signature of upper-mantle plumes: Application to the Northern East African Rift. Geochemistry, Geophysics, Geosystems, 20(12), 6106-6122. https://doi.org/10.1029/2019GC008636

[24] Rooney, T. O., Hanan, B. B., Graham, D. W., Furman, T., Blichert-Toft, J., & Schilling, J. G. (2012). Upper mantle pollution during Afar plume–continental rift interaction. Journal of Petrology, 53(2), 365-389. https://doi.org/10.1093/petrology/egr065

[25] DIGIS Team: GEOROC Compilation: Rift Volcanics (2021). https://doi.org/10.25625/KAIVCT

[26] Chambers, E. L., Harmon, N., Keir, D., & Rychert, C. A. (2019). Using ambient noise to image the northern East African Rift. Geochemistry, Geophysics, Geosystems, 20(4), 2091-2109. https://doi.org/10.1029/2018GC008129

[27] Chambers, E. L., Harmon, N., Rychert, C. A., Gallacher, R. J., & Keir, D. (2022). Imaging the seismic velocity structure of the crust and upper mantle in the northern East African Rift using Rayleigh wave tomography. Geophysical Journal International, 230(3), 2036-2055. https://doi.org/10.1093/gji/ggac156

[28] Benoit, M. H., Nyblade, A. A., & VanDecar, J. C. (2006). Upper mantle P-wave speed variations beneath Ethiopia and the origin of the Afar hotspot. Geology, 34(5), 329-332. https://doi.org/10.1130/G22281.1

[29] Ritsema, J., & Allen, R. M. (2003). The elusive mantle plume. Earth and Planetary Science Letters, 207(1-4), 1-12. https://doi.org/10.1016/S0012-821X(02)01093-2

[30] Hanan, B. B., & Graham, D. W. (1996). Lead and helium isotope evidence from oceanic basalts for a common deep source of mantle plumes. Science, 272(5264), 991-995. https://doi.org/10.1126/science.272.5264.991

[31] Hart, S. R., Hauri, E. H., Oschmann, L. A., & Whitehead, J. A. (1992). Mantle plumes and entrainment: isotopic evidence. Science, 256(5056), 517-520. https://doi.org/10.1126/SCIENCE.256.5056.517

[32] Fitton, J. G., Saunders, A. D., Norry, M. J., Hardarson, B. S., & Taylor, R. N. (1997). Thermal and chemical structure of the Iceland plume. Earth and Planetary Science Letters, 153(3-4), 197-208. https://doi.org/10.1016/S0012-821X(97)00170-2

[33] Pik, R., Marty, B., & Hilton, D. R. (2006). How many mantle plumes in Africa? The geochemical point of view. Chemical Geology, 226(3-4), 100-114. https://doi.org/10.1016/j.chemgeo.2005.09.016

[34] Gallacher, R. J., Keir, D., Harmon, N., Stuart, G., Leroy, S., Hammond, J. O., ... & Ahmed, A. (2016). The initiation of segmented buoyancy-driven melting during continental breakup. Nature Communications, 7(1), 13110. https://doi.org/10.1038/ncomms13110

[35] Abouchami, W., Hofmann, A. W., Galer, S. J. G., Frey, F. A., Eisele, J., & Feigenson, M. (2005). Lead isotopes reveal bilateral asymmetry and vertical continuity in the Hawaiian mantle plume. Nature, 434(7035), 851-856. https://doi.org/10.1038/nature03402

[36] Hutchison, W., Mather, T. A., Pyle, D. M., Boyce, A. J., Gleeson, M. L., Yirgu, G., ... & Finch, A. A. (2018). The evolution of magma during continental rifting: New constraints from the isotopic and trace element signatures of silicic magmas from Ethiopian volcanoes. Earth and Planetary Science Letters, 489, 203-218. https://doi.org/10.1016/j.epsl.2018.02.027

[37] Illsley-Kemp, F., Keir, D., Bull, J. M., Gernon, T. M., Ebinger, C., Ayele, A., ... & Belachew, M. (2018). Seismicity during continental breakup in the Red Sea rift of Northern Afar. Journal of Geophysical Research: Solid Earth, 123(3), 2345-2362. https://doi.org/10.1002/2017JB014902

[38] Hofmann, A. W., Jochum, K. P., Seufert, M., & White, W. M. (1986). Nb and Pb in oceanic basalts: new constraints on mantle evolution. Earth and Planetary science letters, 79(1-2), 33-45. https://doi.org/10.1016/0012-821X(86)90038-5

[39] Armitage, J. J., Ferguson, D. J., Goes, S., Hammond, J. O., Calais, E., Rychert, C. A., & Harmon, N. (2015). Upper mantle temperature and the onset of extension and break-up in Afar, Africa. Earth and Planetary Science Letters, 418, 78-90. https://doi.org/10.1016/j.epsl.2015.02.039

[40] Ebinger, C. J., & Sleep, N. H. (1998). Cenozoic magmatism throughout east Africa resulting from impact of a single plume. Nature, 395(6704), 788-791. https://doi.org/10.1038/27417

[41] Chang, S. J., & Van der Lee, S. (2011). Mantle plumes and associated flow beneath Arabia and East Africa. Earth and Planetary Science Letters, 302(3-4), 448-454.https://doi.org/10.1016/j.epsl.2010.12.050

[42] Hansen, A. H. (2023) "Flow Through Restriction." In Fluid Power Systems: A Lecture Note in Modelling, Analysis and Control, pp. 43-61. Cham: Springer International Publishing. https://doi.org/10.1007/978-3-031-15089-0_4

[43] Naif, S., Miller, N. C., Shillington, D. J., Bécel, A., Lizarralde, D., Bassett, D., & Hemming, S. R. (2023). Episodic intraplate magmatism fed by a long-lived melt channel of distal plume origin. Science Advances, 9(23), eadd3761. https://doi.org/10.1126/sciadv.add3761

[44] Maguire, P. K. H., Keller, G. R., Klemperer, S. L., Mackenzie, G. D., Keranen, K., Harder, S., ... & Amha, M. (2006). Crustal structure of the northern Main Ethiopian Rift from the EAGLE controlled-source survey; a snapshot of incipient lithospheric break-up.

Geological Society, London, Special Publications, 259(1), 269-292. https://doi.org/10.1144/GSL.SP.2006.259.01.21

[45] Lewi, E., Keir, D., Birhanu, Y., Blundy, J., Stuart, G., Wright, T., & Calais, E. (2016). Use of a high-precision gravity survey to understand the formation of oceanic crust and the role of melt at the southern Red Sea rift in Afar, Ethiopia. Special Publications, 420(1), 165-180. https://doi.org/10.1144/SP420.13

Methods

Sample selection and processing

All samples and previously published data used in this study must originate from a volcano that has been active within the Holocene [20] (Fig. 1), with the age of the sample estimated to be of Quaternary age (i.e., < 2.58 Ma). Essential criteria were that the samples are of known (precise) coordinates.

Obtaining previously published data

Previously published geochemical data was obtained from GeoROC [25], [18] and [46]. Once downloaded the data-files were filtered to only include data within Ethiopia (including the Main Ethiopian Rift and Afar). These data were further filtered using the following criteria:

1. The values for the sample must relate to whole rock geochemistry, as opposed to mineral separates.
2. The individual sample must have major element, trace element, $^{87}Sr/^{86}Sr$, $^{143}Nd/^{144}Nd$, $^{206}Pb/^{204}Pb$, $^{207}Pb/^{204}Pb$ and $^{208}Pb/^{204}Pb$ isotope values available.
3. The coordinates must be specific to the individual sample's location rather than providing an average coordinate for a broader study area.

Analytical Geochemistry

Sampling and sample preparation

Ninety-three lavas, eleven welded tuffs and one pumice sample, from various volcanoes in Afar (Erta Ale Volcanic Segment, Ayelu, Abida, Yangudi, Dama Ali, Kerub, Ela, Didoli, Abbahu, Afdera, Tat Ali and Manda Hararo) were selected for geochemical analysis [e.g., 46, 47, 48]. The samples were collected during the CNR/CNRS projects in Afar during the 1960s [49] and stored in the Afar Repository at the University of Pisa, Italy, (http://repositories.dst.unipi.it/index.php/home-afar). A further 52 samples from the Boset-Bericha Volcanic Complex (BBVC) were collected during three field seasons, in November 2012, April-May 2015 [50], and February 2017 [82].

Sample preparation for major, trace and isotope analyses was carried out at the University of Southampton. Samples were cut with a saw to remove any sections, and any cut surfaces ground down to reduce any potential contamination by metals from the saw blade. Rock samples were then crushed using a fly press and placed in double-layered plastic bags prior to crushing to minimise metal contamination.

The crushed material was separated into three size fractions (>1 mm, 0.5 mm to 1 mm, <0.5 mm) using Teflon sieves keeping the middle fraction (0.5 - 1 mm). The selected fraction was cleaned by ultrasonicating in Milli-Q water then dried overnight in an oven at 85ºC. The cleaned rock chips were then hand-picked under a microscope, to remove any non-rock material. An aliquot of cleaned chips were used for Pb isotope analysis. For major element, trace element, and $^{143}Nd/^{144}Nd$ and $^{87}Sr/^{86}Sr$ isotope analysis, the remaining rock chips were ground to a fine powder using an agate mortar and pestle, to minimise contamination with metals.

Trace element analysis

Samples were prepared for whole-rock trace element analysis using 0.05 g (for BBVC samples) or 0.075 g (for all other samples) powdered sample. The powdered samples were digested in sealed Savillex Teflon vials with 15 drops concentrated HNO_3 and 2 ml HF on a hotplate at 130 °C for 24 hours (for all other samples), or with 50 drops HF and 0.2 ml HNO_3 on a hotplate at 130 °C for 24 hours (for BBVC samples). The HNO_3/HF was evaporated off, and the samples were refluxed in 6M HCl for another 24 hours on a hotplate at 130 °C. The 6M HCl was evaporated off, and the samples were redissolved in 6M HCl. Mother solutions were prepared by adding 6M HCl and Milli-Q water (total 30 ml) to the dissolved samples. Daughter solutions were prepared using 0.5 ml of mother solution, diluted to 5 ml with 3% HNO_3 (containing the internal standards 5 ppb In/ 5 ppb Re/ 20 ppb Be), resulting in an overall dilution factor of c. 4000.

Trace element analyses of the daughter samples were undertaken on the Thermo Scientific X Series 2 quadrupole inductively coupled plasma mass spectrometer (ICP-MS) at the University of Southampton. Samples and standards were spiked with internal standard elements and corrected for interferences and blank and then calibrated using a suite of international rock standards. Accuracy was monitored using reference materials JA-2, BCR-2, JB-2 (see Extended Table 3).

Pb isotopic analysis

For Pb isotope analysis, 0.3 g of cleaned, picked rock chips (0.5 mm to 1 mm) were weighed into dedicated Pb Savillex Teflon vials and leached on a hotplate with 4 ml 6M HCl for one hour (15 minutes for obsidian and pumice samples). Samples were rinsed several times in Milli-Q water, then 0.5 ml concentrated HNO_3, before adding 3-4 ml of concentrated HF. Samples were digested as in the trace element section and refluxed on a hotplate at 130 °C for 24 hours, and then evaporated to dryness. 0.5 ml concentrated HCl was added, and the sample evaporated to dryness, then 0.5 ml concentrated HNO_3 was added and again evaporated to dryness. The final residue was reconstituted in 0.5 ml HBr and refluxed for an hour. The samples were cooled and centrifuged for 5 minutes. Pb was isolated using a single-stage HCl anion-exchange chromatographic resin separation method [52], with AGX-1x8, 200 – 400 mesh resin. Following this, the Pb isolate was dried down, redissolved in HNO_3, and analysed using the double spike method of [53]. The samples were subsequently analysed on a Thermo Scientific Neptune Multi-collector inductively coupled plasma mass spectrometer (MC-ICPMS) at the University of Southampton (UK) achieving a NBS SRM 981 reproducibility of $^{206}Pb/^{204}Pb$ = 16.9404 ± 24 (142 ppm), $^{207}Pb/^{204}Pb$ = 15.4969 ± 26 (168 ppm), $^{208}Pb/^{204}Pb$ = 36.7149 ± 66 (180 ppm) (2sd; n=44). Pb isotope measurements of the standard are within error of the accepted values ($^{206}Pb/^{204}Pb$ = 16.9412, $^{207}Pb/^{204}Pb$ = 15.4988, $^{208}Pb/^{204}Pb$ = 36.7233 [45]). Accuracy was 47 ppm for $^{206}Pb/^{204}Pb$, 123 ppm for $^{207}Pb/^{204}Pb$, and 174 ppm for $^{208}Pb/^{204}Pb$.

^{143}Nd/^{144}Nd and ^{87}Sr/^{86}Sr isotopic analysis

For Sr and Nd analysis, remaining mother solutions from the preparation of trace element solutions (see method above) were used for all samples except those of the BBVC. An aliquot of each mother solution was used, to give a volume of liquid containing at least 1 μg Sr and 200 ng Nd and evaporated to dryness in Savillex Teflon vials on a hotplate at 130ºC. Sample residues were reconstituted in 200 μl 1.75M HCl. For the BBVC samples, rock chips were leached in 4 ml 6M HCl or 30 minutes in Savillex Teflon vials (obsidian samples for only 15 minutes, to avoid dissolution of the sample). The samples were then rinsed with Milli-Q water and HNO_3, and then the same digestion procedure as for trace element analysis (above) was followed. The final mother solutions were made up using HCl and Milli-Q water to 30 ml for felsic samples and 20 ml for mafic samples.

All samples were then passed through ion exchange column chemistry, using a AG50-X8 200-400 mesh resin cation column to separate the Sr and Nd fractions. The sample fractions were subsequently evaporated to dryness ready for further column chemistry.

Sr was further isolated through Sr-spec resin column, following the methodology of [54]. Samples were then evaporated to dryness, dissolved in 1.5 ml 1M HCl and loaded onto outgassed tantalum filaments with 1 μl of Ta-activator. Sr isotopic analysis was performed on a Thermal Ionisation Mass Spectrometer (TIMS) Thermo Scientific Triton Plus at the

University of Southampton. Reference material SRM NIST987 ($^{87}Sr/^{86}Sr$ = 0.710258; GeoREM) was used to monitor accuracy and gave average $^{87}Sr/^{86}Sr$ values of 0.710243 and samples are quoted relative to 0.710248, while reproducibility was ± 0.000020 (28.2 ppm, 2sd; n=464). Accuracy was 21 ppm.

The Nd aliquot from the cation column was followed by an Ln-spec resin (50-100 μm) [55]. The samples were then evaporated to dryness and 3% HNO_3 was added to produce a solution of 50 ppb. $^{143}Nd/^{144}Nd$ analyses were undertaken on the ThermoScientific Neptune multi-collector inductively coupled plasma mass spectrometer (MC-ICP-MS) at the University of Southampton. Corrected Nd isotopic compositions were obtained using a method based on [56] through adjustment to a $^{146}Nd/^{144}Nd$ ratio of 0.7219 and a secondary normalisation to $^{142}Nd/^{144}Nd$ = 1.141876. Reference material JNdi-1 was measured as an unknown ($^{143}Nd/^{144}Nd$ of 0.512124, 2sd; [57]) achieving an average $^{143}Nd/^{144}Nd$ of 0.512115 with an external reproducibility of ±0.000008 (2sd, 15.2 ppm) across 6 analysis sessions over 2 years. The total column blanks (i.e., when blank acid is run through the column procedure) were negligible (<20 pg) compared to the total amounts analysed (1 μg and 200 μg) for Sr and Nd, respectively.

Geophysical analyses

Shear velocity maps from joint inversion of teleseismic and ambient noise Rayleigh-wave phase velocities

We use the shear wave velocity model of [27] for the analysis. The 3D velocity model is created through a joint inversion of Rayleigh-wave phase-velocities from ambient noise and teleseisms [26, 27]. The shear velocity model is parameterised every 5 km vertically with 0.1° x 0.1° pixel size for the upper 50 km. For deeper depths, an irregular spacing was used, increasing from 10 – 50 km spacings to match that of [34]. For further details on creation of the velocity model, see [26, 27] and references therein.

For the analysis in this paper, the shear velocity model was interpolated to 1 km depth using a linear interpolation; we then extracted 1D columns of velocity with depth at the same resolution as our pixel size.

Moho depths

The gridded Moho depth map was produced from the Vs maps of [26] described above. The Vs model was interpolated to a vertical grid spacing of 1 km and a velocity slice at the 3.75 km/s contour was extracted which mapped best to previous receiver function measurements [58-62], active source experiments (e.g., [63]) and previous S-wave models (e.g., [64]).

Statistical analysis

Models considered

Five models were considered (see Extended Data Table 1), with each model being tested using a linear fit and a spline fit (Fig. 2). We note that a spline fit to itself can be linear if that is the best-fitting line.

Empirical models are estimated for the variation of each of 13 geochemical quantities (each of which is represented generically by random variable Y) as a function of distance $d \in [0, 1800]$ km for five different models. Models are specified that explore the variation of Y with d in increasing complexity. The simplest model (C1C) assumes the existence of a single upwelling centre (at 11.192 ºN 41.784 ºE, Fig. 1), with respect to which d is defined for all three rifts; the variation of Y with d is assumed common to all rifts. Model C3C assumes the existence of three upwelling centres (at 11.192 ºN 41.784 ºE, 14.008 ºN 40.458 ºE & 6.626 ºN 37.948 ºE, Fig. 1) based on [23]; observations are allocated to the nearest upwelling centre, facilitating calculation of a single d for each observation; like model C1C, the variation of Y with d is assumed common to all rifts, regardless of upwelling allocation. Model C1D assumes one upwelling centre (like C1C) for calculation of d, but now the variation of Y with d is assumed to be different across rifts. Model C3D duplicates C3C for estimation of d, but variation of Y with d is assumed to be different across rifts. Finally, in model C3X we consider the presence of three upwelling centres, with different variation of Y with d for each combination of upwelling and rift.

Data pre-processing

For models C1C and C1D, the distance between each sample and the upwelling locus centred on Lake Abhe (11.192170 ºN 41.783750 ºE) is calculated. For models C3C, C3D and C3X, the distance between each sample and each of the three upwelling locations (Fig. 1) is measured, and then each sample is assigned to its nearest upwelling centre. The distance (*d*) between two locations (i.e., upwelling and sample) is calculated using the spherical cosine law:

$$d = R(\cos^{-1}(\cos(a)\cos(b) + \sin(a)\sin(b)\cos(C)) \qquad \text{(Eq. 5)}$$

where *a* is the angle (in radians) from the North Pole to the sample location, *b* is the angle (in radians) from the North Pole to the upwelling location, *C* is the difference in radians between the longitude values of the sample and upwelling, and *R* is the radius of the earth in meters (6371×10^3).

Penalised B-splines

For each model, the variation of *Y* with *d* (possibly for a subset of the full sample) is described using a penalised B-spline (e.g., [65, 66]), the characteristics of which are selected to provide optimal predictive performance. First, for a large index set of locations equally spaced on the domain of distance, we calculate a B-spline basis matrix, *B* (e.g., [67]) consisting of p equally spaced cubic spline basis functions. Then the value of Y on the index set is given by the vector $B\beta$, for spline coefficient vector β to be estimated. The value of p is specified to be sufficiently large to provide a good description of a highly variable Y. For a given data set, we penalise the difference between consecutive values in β using a roughness penalty, such that the penalised spline exhibits optimal roughness providing optimal predictive performance.

Estimating optimal spline roughness and predictive performance

For a sample of n_1 training data, consisting of vectors of geochemical quantities (y_1) and distances (d_1), we first allocate each element of d_1 to its nearest neighbour in the index set, and hence construct the appropriate spline basis matrix B_1 for the sample. We then assume that $y_1 = B_1\beta + \varepsilon$, where the elements of ε are independently and identically distributed zero-mean Gaussian random variables. We penalise the roughness of β using a first-different penalty $\lambda\beta' P\beta$, where $P = D'D$ and D is a first difference matrix (with elements $D_{ij} = -1$ if $i = j; = 1$ if $j = i + 1$; and $= 0$ otherwise (e.g., [68]). For a given choice of λ, we then find the optimal value of β by minimising lack of fit:

$$\beta^*(\lambda) = \underset{\beta}{argmin}\{(y_1 - B_1\beta)'(y_1 - B_1\beta) + \lambda\beta' P\beta\} \qquad \text{(Eq. 6)}$$

$$= (B_1' B_1 + \lambda P)^{-1} B_1' y_1 \qquad \text{(Eq. 7)}$$

We can evaluate the predictive performance of the resulting spline description using a tuning set of n_2 observations (independent of the training set) represented by vectors y_2 and d_2. We again start by finding the appropriate spline basis matrix B_2 for this sample. Then we can calculate the predictive mean square error for the tuning sample

$$\mathrm{MSE}_{Tune}(\lambda) = \frac{1}{n_2}\left(y_2 - B_2\beta^*(\lambda)\right)'\left(y_2 - B_2\beta^*(\lambda)\right) \qquad \text{(Eq. 8)}$$

for each of a set of representative choices of values for λ. We can then select the optimal value of λ using

$$\lambda^* = \underset{\lambda}{argmin}\,\{\mathrm{MSE}_{Tune}(\lambda)\} \quad \text{(Eq. 9)}$$

The value $\mathrm{MSE}_{Tune}(\lambda^*)$ is a biased estimate of predictive performance since the value of λ^* was tuned to minimise its value. We can obtain an unbiased estimate for the predictive performance of the spline model using a test set of n_3 observations (independent of the training and tuning sets) represented by vectors y_3 and d_3 (and corresponding spline basis matrix B_3). Then the predictive performance is estimated using:

$$MSE_{Test} = \frac{1}{n_3}\left(y_3 - B_3\beta^*(\lambda^*)\right)'\left(y_3 - B_3\beta^*(\lambda^*)\right) \quad \text{(Eq. 10)}$$

Cross-validation and model comparison

We exploit cross-validation to evaluate MSE_{Test}, by partitioning the full sample of data into $k > 2$ groups at random, withholding one group for tuning, another group for testing, retaining the remaining $k - 2$ groups for training. We then loop exhaustively over all possible combinations of choice of train, tune, and test groups, evaluating overall predictive performance on the test data over all iterations, noting that each observation occurs exactly once in the test set. For models (that is, C1D, C3D, C3X) requiring separate model fits to subsets of data, MSE_{Test} is estimated using predictions from optimal predictive models for each subset. Further, we can repeat the analysis for different initial random partitioning of observations into k groups, to assess the sensitivity of overall predictive performance to this choice. We are careful to use the same cross-validation partitions to evaluate each of the five models, so that predictive performances can be compared fairly.

To quantify model performance over all 13 geochemical quantities ($j = 1,2,\dots,13$), we define the overall standardised MSE_{Test}

$$\mathrm{SMSE} = \sum_{j=1}^{13} \frac{\mathrm{MSE}_{Test,j}}{s_j^2} \qquad \text{(Eq. 11)}$$

where $\mathrm{MSE}_{Test,j}$ is the predictive performance for the *j*th geochemical indicator, and s_j^2 is the sample estimate for the variance of that quantity. The estimation of the splines and the testing of their predictive performance was repeated over 100 iterations. Results from each iteration and the mean of the SMSE is shown in Fig. 3.

Linear regression

For comparison, we also evaluate linear regression models for the variation of *Y* with *d*. In the current notation, these can be thought of as simple models with basis matrix $B = [1\ d]$, where *1* is a vector of appropriate length with each element = *1*. *B* in this case is a 2-vector with elements corresponding to intercept and slope coefficients. Linear regression is approached using penalised B-spline models as the roughness coefficient $\lambda \rightarrow \infty$. That is, linear regression corresponds to a penalised B-spline model with very large λ. Therefore, a penalised B-spline model is guaranteed to perform at least as well as linear regression.

Principal component analysis

Principal component analysis (PCA) requires each sample or object to have the same number of values for each variable and so the dataset was reduced to 94 samples. PCA is only carried out on radiogenic isotope compositions of the samples where data are available for the mantle end members investigated (i.e., Afar plume, Pan-African Lithosphere, Depleted Mantle, Enriched Mantle 1, Enriched Mantle 2, HiMU, Extended Fig. 4). Values used for the end members is provided in Extended Table 4. Each object is standardised before being included in the PCA:

$$y_{\mathrm{std}j} = \frac{y_j - \bar{y}_j}{\sigma_j} \quad \text{(Eq. 12)}$$

where $\bar{y}_j$ is the mean of variable j, and σ_j is the standard deviation of the variable j:

$$\sigma_j = \sqrt{\frac{\Sigma\{(y_j - \bar{y}_j)\}^2}{N_j}} \quad \text{(Eq. 13)}$$

where N_j is the number of objects within variable j.

Approximately 90.5% of the variance is explained within the plane of the first two eigenvectors, increasing to 95.5% when including the third eigenvector. The first principal component (PC-1) is most influenced by $^{207}Pb/^{204}Pb$, $^{208}Pb/^{204}Pb$, whereas the second principal component (PC-2) is dominantly influenced by $^{206}Pb/^{204}Pb$ and $^{87}Sr/^{86}Sr$. The third principal component (PC-3) is dominated by $^{207}Pb/^{204}Pb$ and $^{143}Nd/^{144}Nd$ (Extended Data Table 5).

K-means cluster analysis

K-means cluster analysis [69] is carried out on the samples using the 13 standardised variables, which are $^{206}Pb/^{204}Pb$, $^{207}Pb/^{204}Pb$, $^{208}Pb/^{204}Pb$, $^{143}Nd/^{144}Nd$, $^{87}Sr/^{86}Sr$, Ce/Pb, La/Sm, ΔNb, shear-wave speed at 40 km, 60 km, 80 km, 100 km, and 120 km depths. The K-means algorithm assigns each object to a singular cluster that does not overlap with another (i.e., partitional clustering), minimising the total sum of squared error (SSE) from the centre point of each cluster, known as the centroid, to each object.

To find the optimum number of clusters (k), i.e., which reduces the within-cluster total sum of squares error with the lowest number of clusters, we run the K-means algorithm specifying k to be 1:20, over 1000 iterations for each k (Extended Fig. 3). We then select eight clusters based on $k=8$ reducing the within-cluster total sum of squares by 75% from $k=1$, and the range over the 1,000 iterations being minimised when $k \geq 8$. The cluster assignments for each object, out of the 1,000 iterations, are selected by finding the iteration number that is closest to the mean within-cluster total sum of squares of that *k* value (shown by the blue line in Extended Fig. 3).

Data Availability

The datasets analysed for the current project are available as Supplementary Material. Some data was obtained from GeoROC [25], [18] and [46], however this data is clearly marked and included in the datafile.

Code Availability

The input data, code and output within this study can be found freely available on https://github.com/ygraigarw/AfarPlume.git.

Methods References

[46] Watts, E. J., Gernon, T. M., Taylor, R. N., Keir, D., & Pagli, C. (2023). Magmatic evolution during proto-oceanic rifting at Alu, Dalafilla and Borale Volcanoes (Afar) determined by trace element and Sr-Nd-Pb isotope geochemistry. Lithos, 456, 107311. https://doi.org/10.1016/j.lithos.2023.107311

[47] Watts, E. J., Gernon, T. M., Taylor, R. N., Keir, D., Siegburg, M., Jarman, J., ... & Gioncada, A. (2020). Evolution of the Alu-Dalafilla and Borale volcanoes, Afar, Ethiopia. Journal of Volcanology and Geothermal Research, 408, 107094. https://doi.org/10.1016/j.jvolgeores.2020.107094

[48] Rees, R., Gernon, T. M., Keir, D., Taylor, R. N., & Pagli, C. (2023). The spatial and volcanic evolution of Ayelu, Abida and Yangudi volcanoes in the Northern Main Ethiopian Rift–Southern Afar, Ethiopia. Journal of Volcanology and Geothermal Research, 440, 107846. https://doi.org/10.1016/j.jvolgeores.2023.107846

[49] Barberi, F., & Varet, J. (1970). The Erta Ale volcanic range (Danakil depression, northern afar, ethiopia). Bulletin Volcanologique, 34, 848-917. https://doi.org/10.1007/BF02596805

[50] Siegburg, M., Gernon, T. M., Bull, J. M., Keir, D., Barfod, D. N., Taylor, R. N., ... & Ayele, A. (2018). Geological evolution of the Boset-Bericha volcanic complex, Main Ethiopian Rift: $^{40}Ar/^{39}Ar$ evidence for episodic Pleistocene to Holocene volcanism. Journal of Volcanology and Geothermal Research, 351, 115-133. https://doi.org/10.1016/j.jvolgeores.2017.12.014

[51] Siegburg, M., Gernon, T. M., Keir, D., Bull, J. M., Taylor, R. N., Watts, E. J., ... & Gebru, E. F. (2023). Temporal clustering of fissural eruption across multiple segments within

the Ethiopian Rift. Frontiers in Earth Science, 11, 1169635. https://doi.org/10.3389/feart.2023.1169635

[52] Kamber, B. S., & Gladu, A. H. (2009). Comparison of Pb purification by anion-exchange resin methods and assessment of long-term reproducibility of Th/U/Pb ratio measurements by quadrupole ICP-MS. Geostandards and Geoanalytical Research, 33(2), 169-181. https://doi.org/10.1111/J.1751-908X.2009.00911.X

[53] Taylor, R. N., Ishizuka, O., Michalik, A., Milton, J. A., & Croudace, I. W. (2015). Evaluating the precision of Pb isotope measurement by mass spectrometry. Journal of Analytical Atomic Spectrometry, 30(1), 198-213. https://doi.org/10.1039/c4ja00279b

[54] Pin, C., Briot, D., Bassin, C., & Poitrasson, F. (1994). Concomitant separation of strontium and samarium-neodymium for isotopic analysis in silicate samples, based on specific extraction chromatography. Analytica Chimica Acta, 298(2), 209-217. https://doi.org/10.1016/0003-2670(94)00274-6

[55] Pin, C., & Zalduegui, J. S. (1997). Sequential separation of light rare-earth elements, thorium, and uranium by miniaturized extraction chromatography: application to isotopic analyses of silicate rocks. Analytica Chimica Acta, 339(1-2), 79-89. https://doi.org/10.1016/S0003-2670(96)00499-0

[56] Vance, D., & Thirlwall, M. (2002). An assessment of mass discrimination in MC-ICPMS using Nd isotopes. Chemical Geology, 185(3-4), 227-240. https://doi.org/10.1016/S0009-2541(01)00402-8

[57] Tanaka, T., Togashi, S., Kamioka, H., Amakawa, H., Kagami, H., Hamamoto, T., ... & Dragusanu, C. (2000). JNdi-1: a neodymium isotopic reference in consistency with LaJolla neodymium. Chemical Geology, 168(3-4), 279-281. https://doi.org/10.1016/S0009-2541(00)00198-4

[58] Hammond, J. O., Kendall, J. M., Stuart, G. W., Keir, D., Ebinger, C., Ayele, A., & Belachew, M. (2011). The nature of the crust beneath the Afar triple junction: Evidence from receiver functions. Geochemistry, Geophysics, Geosystems, 12(12). https://doi.org/10.1029/2011GC003738

[59] Ayele, A., Stuart, G., & Kendall, J. M. (2004). Insights into rifting from shear wave splitting and receiver functions: An example from Ethiopia. Geophysical Journal International, 157(1), 354-362. https://doi.org/10.1111/j.1365-246X.2004.02206.x

[60] Dugda, M. T., Nyblade, A. A., Julia, J., Langston, C. A., Ammon, C. J., & Simiyu, S. (2005). Crustal structure in Ethiopia and Kenya from receiver function analysis: Implications for rift development in eastern Africa. Journal of Geophysical Research: Solid Earth, 110(B1). https://doi.org/10.1029/2004JB003065

[61] Ogden, C. S., Bastow, I. D., Gilligan, A., & Rondenay, S. (2019). A reappraisal of the H–κ stacking technique: implications for global crustal structure. Geophysical Journal International, 219(3), 1491-1513. https://doi.org/10.1093/gji/ggz364

[62] Stuart, G. W., Bastow, I. D., & Ebinger, C. J. (2006). Crustal structure of the northern Main Ethiopian Rift from receiver function studies. Geological Society, London, Special Publications, 259(1), 253-267. https://doi.org/10.1144/GSL.SP.2006.259.01.20

[63] Maguire, P. K. H., Keller, G. R., Klemperer, S. L., Mackenzie, G. D., Keranen, K., Harder, S., ... & Amha, M. (2006). Crustal structure of the northern Main Ethiopian Rift from the EAGLE controlled-source survey; a snapshot of incipient lithospheric break-up. Geological Society, London, Special Publications, 259(1), 269-292. https://doi.org/10.1144/GSL.SP.2006.259.01.21

[64] Keranen, K. M., Klemperer, S. L., Julia, J., Lawrence, J. F., & Nyblade, A. A. (2009). Low lower crustal velocity across Ethiopia: Is the Main Ethiopian Rift a narrow rift in a hot

craton?. Geochemistry, Geophysics, Geosystems, 10(5). https://doi.org/10.1029/2008GC002293

[65] Eilers, P. H., & Marx, B. D. (1996). Flexible smoothing with B-splines and penalties. Statistical science, 11(2), 89-121. https://doi.org/10.1214/ss/1038425655

[66] Eilers, P. H., & Marx, B. D. (2010). Splines, knots, and penalties. Wiley Interdisciplinary Reviews: Computational Statistics, 2(6), 637-653. https://doi.org/10.1002/wics.125

[67] De Boor, C., (1978). A practical guide to splines Vol. 27 Springer-verlag. New York. https://doi.org/10.1007/978-1-4612-6333-3

[68] Jones, M., Randell, D., Ewans, K., & Jonathan, P. (2016). Statistics of extreme ocean environments: Non-stationary inference for directionality and other covariate effects. Ocean Engineering, 119, 30-46. https://doi.org/10.1016/j.oceaneng.2016.04.010

[69] Arthur, D., & Vassilvitskii, S. (2007). k-means++: The advantages of careful seeding. In Soda (Vol. 7, pp. 1027-1035).https://doi.org/10.5555/1283383

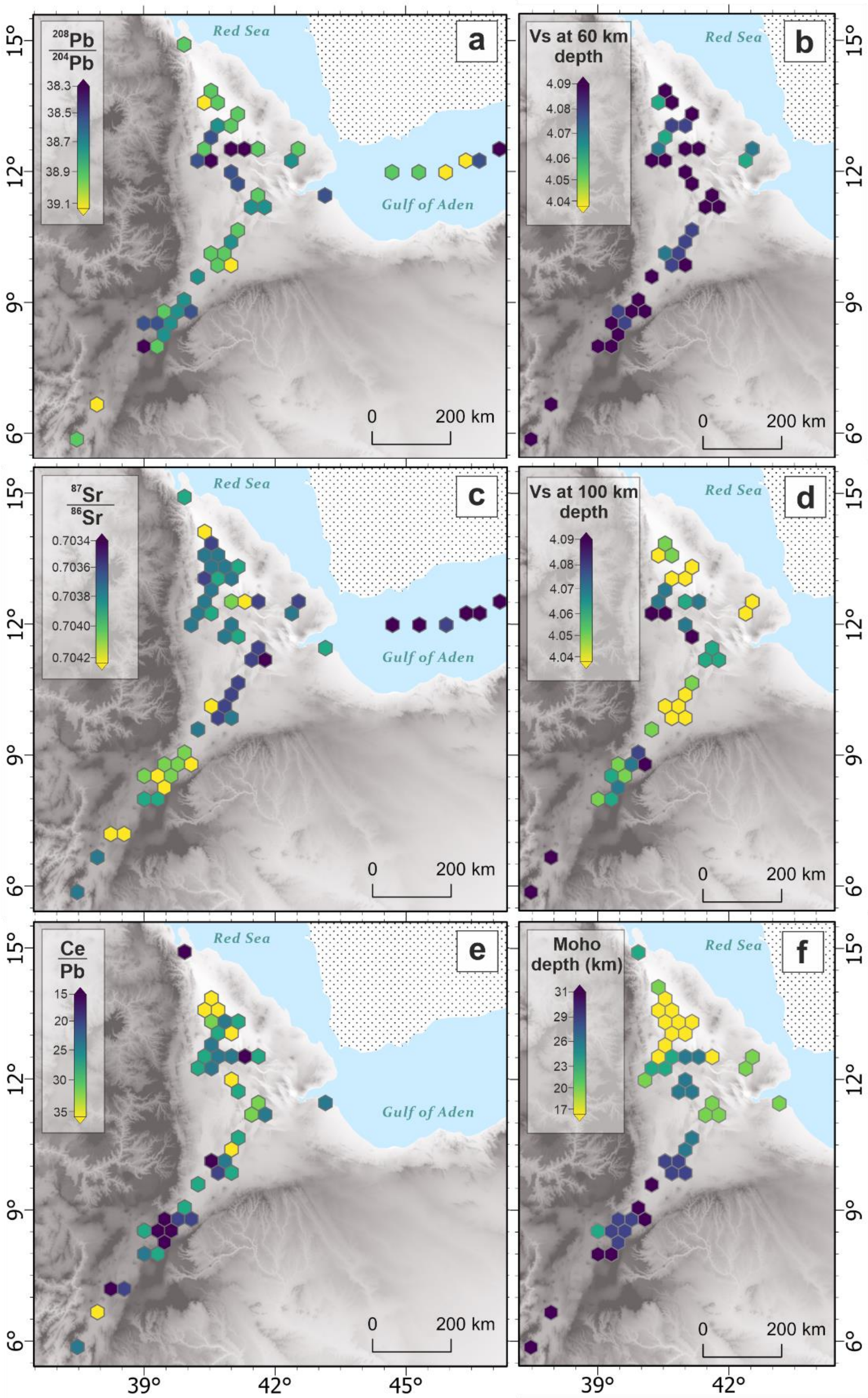

Extended Data Fig. 1: Hexmaps showing the patterns for the selected variables (see Manuscript and Extended Table 2 for further details) across the study region. (a) ^{208}Pb/^{204}Pb; (b) Shear wave velocity (Vs) at 60 km depth; (c) ^{87}Sr/^{86}Sr; (d) Shear wave velocity (Vs) at 100 km; (e) Ce/Pb; (f) Moho depth (km).

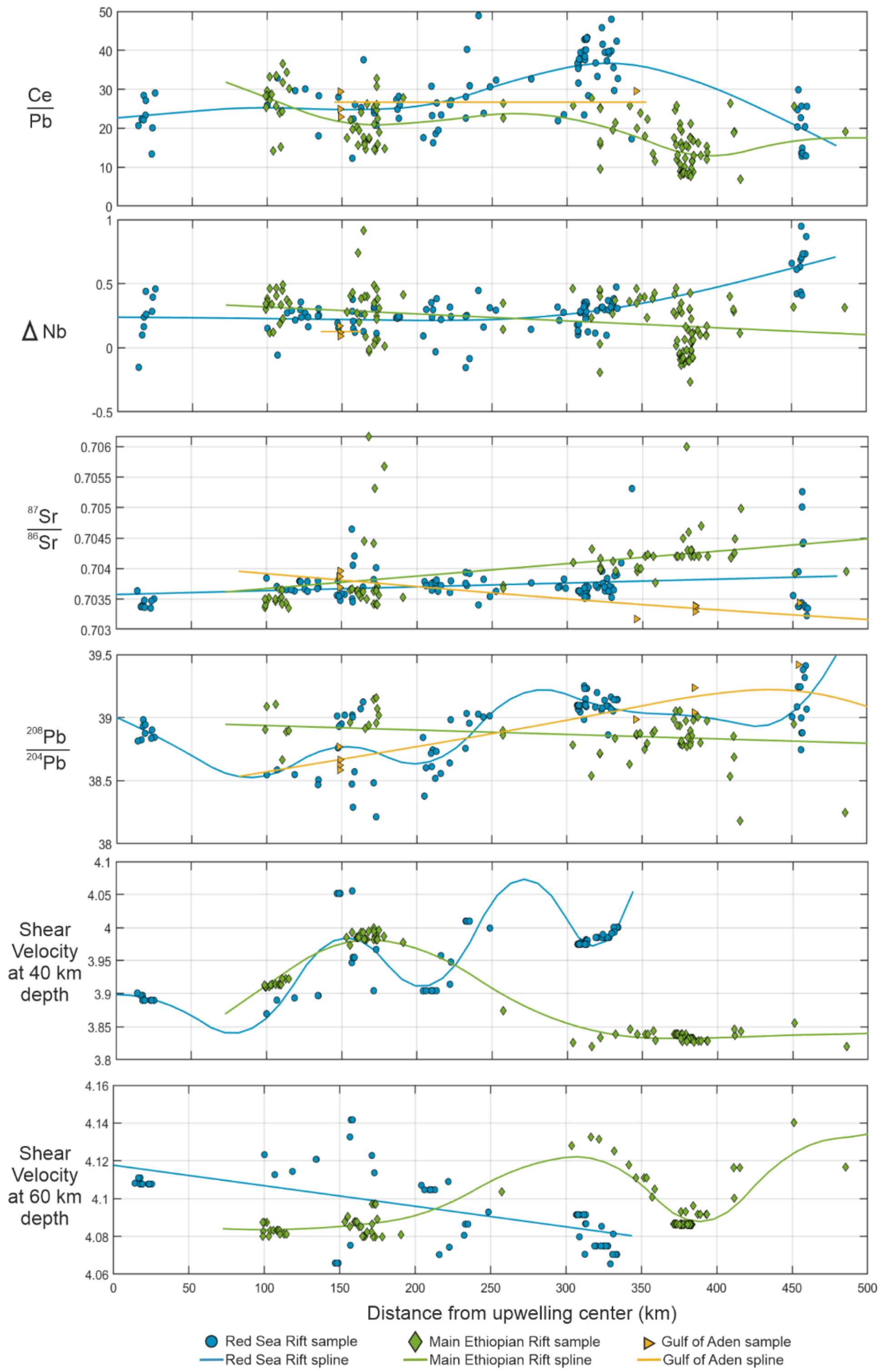

Extended Data Fig. 2 Splines of the winning model (C1C) for remaining selected variables not shown in Figure 3. Symbols show the data within the study (blue circles = Red Sea Rift, green diamonds = Main Ethiopian Rift, yellow triangles = Gulf of Aden Rift). Standard deviation (2sd) for the data points is smaller than the symbols used.

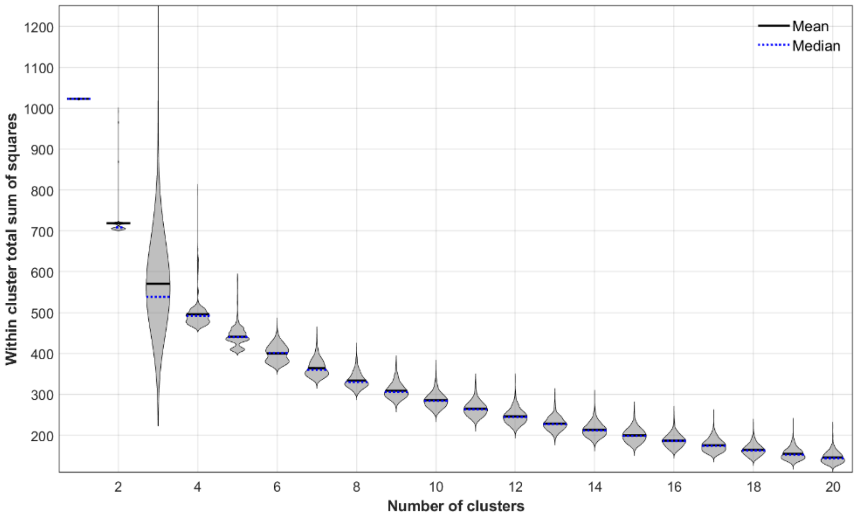

Extended Data Fig. 3 (a) Violin plot showing the within cluster sum of squares for the k–means cluster analysis testing number of clusters between 1 and 20, for 1000 iterations.

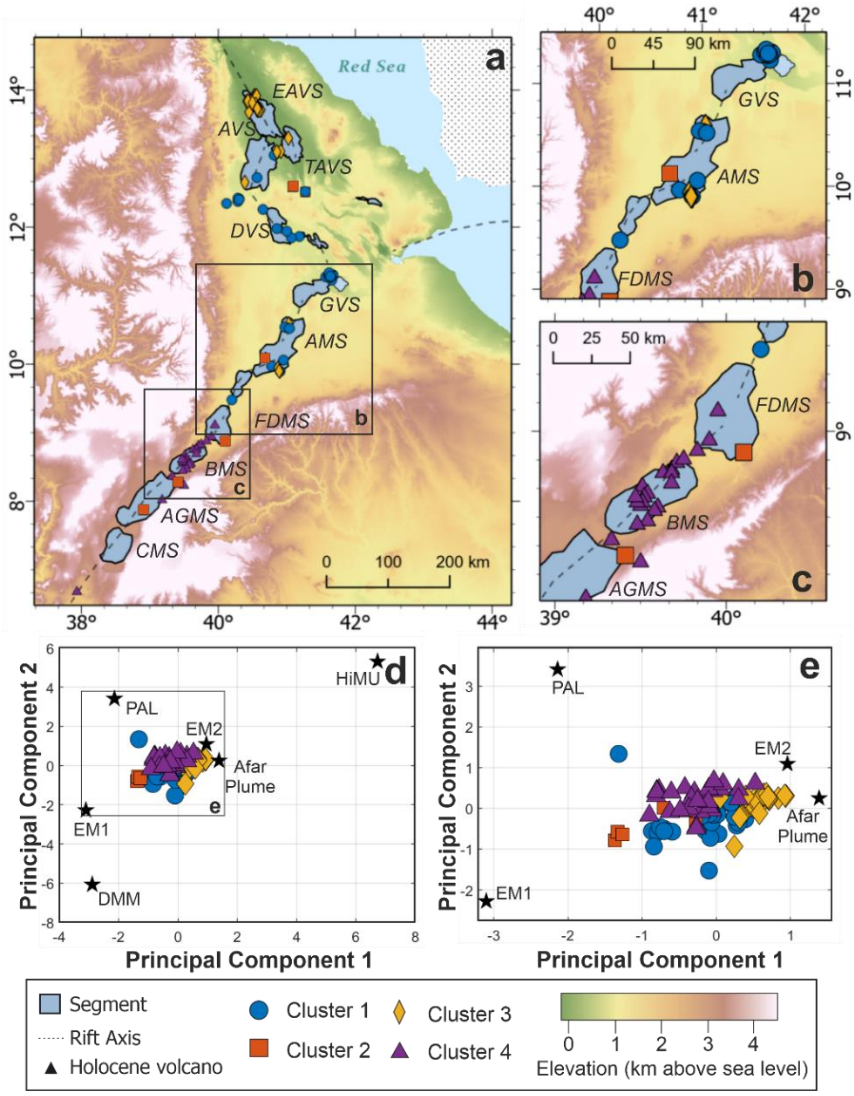

Extended Data Fig. 4: Map of the segments and cluster assignment (see legend) within the study region. Segments are shown in blue from north to south: Erta Ale Volcanic Segment (EAVS), Tat'Ale Volcanic Segment (TAVS), Alayta Volcanic Segment (AVS), Dabbahu Volcanic Segment (DVS), Gabillema Volcanic Segment (GVS), Adda'do Magmatic Segment (AMS), Fentale-Dofen Magmatic Segment (FDMS), Boset Magmatic Segment (BMS), Aluto-Gedamsa Magmatic Segment (AGMS), Corbetti Magmatic Segment (CMS). Rift axis (dotted line) and Holocene volcanoes (black triangles) are shown. (b) and (c) are enlarged maps of the boxes shown in (a). (d) & (e) Principal component analysis bi-plot (PC1 vs PC2) when considering the six isotopic systems (see Manuscript and Extended Table 2) showing the samples and their component scores relative to those of the mantle end-members. Value used for the Mantle end members – Pan-African Lithosphere (PAL), Enriched Mantle 1 & 2 (EM1, EM2 respectively), Depleted MORB Mantle (DMM) and HiMU – are shown in Extended Table 4.

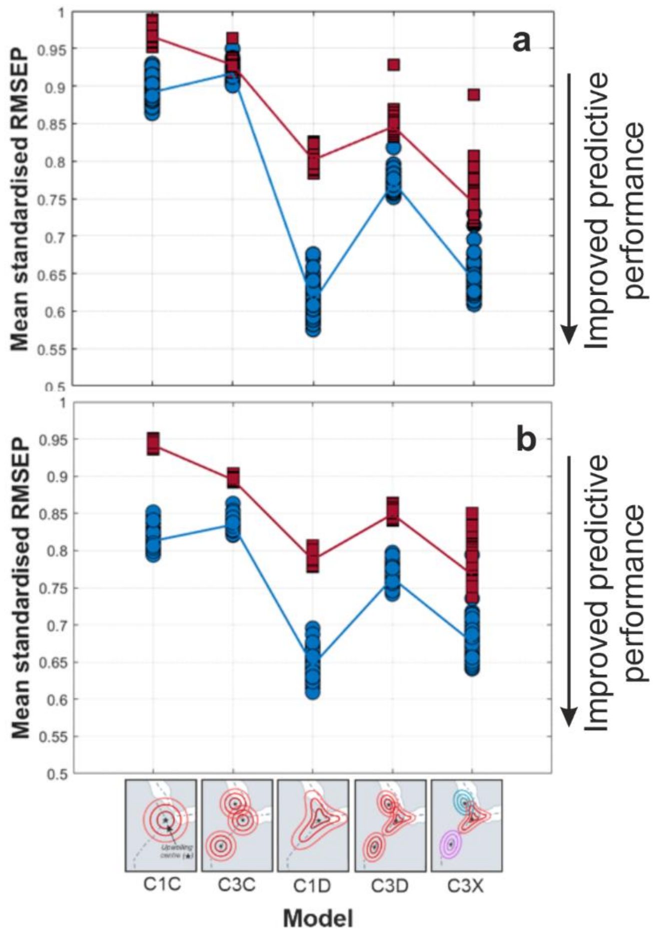

Extended Data Fig. 5: The mean standardised root means square error of prediction (RMSEP) for each of the models tested (see Extended Table 1) when (a) excluding any observations that have a Ce/Pb > 20 (b) excluding the Gulf of Aden. In both plots individual linear model results are shown by red squares and the mean of those results are displayed by the red line. Individual spline results are shown by blue circles and the mean of those results are shown by a blue line.

Model	Description
C1C	A singular upwelling centred at Lake Abhe (11.192 ºN 41.784 ºE) with each rift (i.e., Red Sea Rift, Gulf of Aden rift and Main Ethiopian Rift) behaving the same (not independent), based on the theory of [5]. This model fits a single line using all the data points from each rift.
C3C	Three upwellings centred at Lake Abhe (11.192 ºN 41.784 ºE), and two other points across the region (14.008 ºN 40.458 ºE & 6.626 ºN 37.948 ºE); a model based on the locations of previously proposed small-scale upwelling locations through numerical modelling [23]. Assumes each rift behaves the same (not independent of each other) and the upwellings are of the same composition. This model fits a single line across all the data points.
C1D	A singular upwelling centred at Lake Abhe (11.192 ºN 41.784 ºE) with each rift behaving independently. This model fits three lines (one for each rift) across the data points for the corresponding rift.
C3D	Three small-scale upwellings centred at Lake Abhe (11.192 ºN 41.784 ºE), and two other points across the region (14.008 ºN 40.458 ºE & 6.626 ºN 37.948 ºE) with each rift acting independently. This model assumes each upwelling is compositionally the same and fits three lines (one for each rift) across the data points for the corresponding rift.
C3X	Three small-scale upwellings centred at Lake Abhe (11.192 ºN 41.784 ºE), and two other points across the region (14.008 ºN 40.458 ºE & 6.626 ºN 37.948 ºE) with each rift and upwelling acting independently. This model plots five lines.

Extended Data Table 1: Models considered when assessing the upwelling characteristics in Afar.

Variable (s)	Observed Range	Details
$^{206}Pb/^{204}Pb$	17.853 to 19.608	$^{206}Pb/^{204}Pb$ >20 is linked to HIMU, $^{206}Pb/^{204}Pb$ ranging from 19.2 to 20.5 indicates a mantle upwelling source (C, FOZO) [70] and $^{206}Pb/^{204}Pb$ <17.8 can be related to a depleted mantle component [71, 72].
$^{207}Pb/^{204}Pb$	15.448 to 15.697	$^{207}Pb/^{204}Pb$ <15.5 is related to a depleted mantle component [70], $^{207}Pb/^{204}Pb$ >15.65 is linked to the HiMU component and $^{207}Pb/^{204}Pb$ ~ 15.6 indicates a mantle upwelling source (C, FOZO). A $^{207}Pb/^{204}Pb$ >15.75 is linked to crustal values [18, 24].
$^{208}Pb/^{204}Pb$	37.984 to 39.420	$^{208}Pb/^{204}Pb$ <38 is related to a depleted mantle component [70], $^{208}Pb/^{204}Pb$ >39.5 is linked to the HiMU component and $^{208}Pb/^{204}Pb$ 39.2 to 39.5 indicates a mantle upwelling source (C, FOZO). A $^{208}Pb/^{204}Pb$ >39.7 is linked to crustal values [18, 24].
$^{143}Nd/^{144}Nd$	0.51259 to 0.51317	A low $^{143}Nd/^{144}Nd$ (<0.5121) indicates continental crust or Pan African Lithosphere. $^{143}Nd/^{144}Nd$ values ~ 0.51285 indicates a HIMU or upwelling related mantle source. Higher $^{143}Nd/^{144}Nd$ values (>0.5131) indicate a depleted mantle source (i.e., DMM) [18, 71-73].
$^{87}Sr/^{86}Sr$	0.70280 to 0.70678	A low $^{87}Sr/^{86}Sr$ (0.7040-0.7045) indicates a mantle component that is either depleted (DMM) or an upwelling (HIMU, C). A higher $^{87}Sr/^{86}Sr$ (<0.705) indicates the potential influence from continental crust [18, 71-73].
Ce/Pb	6.84 to 48.92	A Ce/Pb >30 is commonly attributed to a recycled mantle source that has been depleted in fluid mobile elements (i.e., Pb, Ba, Sr, K) during subduction, therefore resulting in high fluid-immobile-element to fluid-mobile-element ratios (i.e., Ce/Pb). Typical mantle has a Ce/Pb value of 25±5 and crust a value of ~4 [38].
La/Sm	0.4 to 4.7	(La/Sm) >1 indicates LREE enrichment fractionation (alkali basalts or upwelling), (La/Sm) <1 indicates LREE depleted (mid-ocean ridge). The higher the La/Sm the lower the melt fraction [5]
ΔNb	-0.26 to 0.95	Differentiates between a depleted mantle (ΔNb <0) and a mantle upwelling (ΔNb >0) [29]. $$\Delta Nb = 1.74 + log\left(\frac{Nb}{Y}\right) - 1.92\ log\left(\frac{Zr}{Y}\right)$$
Vs @ 40 km	3.81 to 4.06	Shear wave velocities can be sensitive, temperature, grainsize and the presence of fluids. A reduction in Vs can indicate a change in mantle composition or an increased proportion of melt/hydrothermal fluid [26]. This is the velocity from 40 km depth.
Vs @ 60 km	4.06 to 4.18	
Vs @ 80 km	4.00 to 4.16	
Vs @ 100 km	3.97 to 4.10	
Vs @ 120 km	4.03 to 4.10	
Moho depth	16-30 km	Depth to the Mohorovičić Discontinuity.

Extended Data Table 2: Variables used within the analysis summarising the ranges observed and justifying their selection.

	JA-2 (Imai et al., 1995), n=6					BCR-2 (Wilson., 1997), n=4					JB-2 (GeoREM), n=3					
	Mean	**Std.Dev**	**%RSD**	**Ref.**	**Uncert.**	**Mean**	**Std.Dev**	**%RSD**	**Ref.**	**Uncert.**	**Mean**	**Std.Dev**	**%RSD**	**Ref.**	**Uncert.**	**Accuracy %**
Li	29.41	0.25	0.85	29.18	0.60	9.04	0.12	1.33	9.13	0.22	8.16	0.16	1.96	8.08	0.15	0.99
Sc	17.91	0.19	1.06	18.93	0.30	32.55	0.17	0.52	33.53	0.40	55.35	0.52	0.94	54.08	0.76	2.35
V	115.38	4.32	3.74	119.70	2.40	403.50	5.06	1.25	417.60	4.50	575.27	9.98	1.73	572.40	8.30	0.50
Cr	397.18	13.36	3.36	424.80	9.30	14.56	0.47	3.23	15.85	0.38	24.63	0.31	1.26	26.65	0.69	7.58
Co	27.55	0.20	0.73	28.33	1.00	36.86	0.19	0.52	37.33	0.37	37.18	0.58	1.56	37.57	0.67	1.04
Ni	127.20	1.68	1.32	136.00	2.20	11.72	0.41	3.50	12.57	0.30	13.65	0.29	2.12	14.77	0.51	7.58
Cu	30.36	0.97	3.19	29.00	1.50	23.06	1.24	5.38	19.66	0.72	222.63	2.76	1.24	222.10	3.60	0.24
Rb	72.17	1.29	1.79	69.80	1.30	46.46	0.92	1.98	46.02	0.56	6.24	0.25	4.01	6.40	0.11	2.50
Sr	245.67	1.43	0.58	245.80	3.00	333.78	1.47	0.44	337.40	6.70	175.90	2.21	1.26	178.20	1.50	1.29
Y	17.17	0.07	0.41	16.89	0.60	36.01	0.09	0.25	36.07	0.37	23.89	0.28	1.17	23.56	0.44	1.40
Zr	114.72	0.75	0.65	108.50	2.60	187.65	1.74	0.93	186.50	1.50	45.42	0.40	0.88	48.25	0.88	5.87
Nb	9.24	0.10	1.08	9.30	0.20	12.43	0.24	1.93	12.44	0.20	0.49	0.00	0.00	0.57	0.03	13.27
Cs	4.97	0.11	2.21	4.78	0.10	1.11	0.04	3.60	1.16	0.13	0.77	0.02	2.60	0.80	0.02	3.75
Ba	317.67	5.45	1.72	308.40	5.10	692.20	12.06	1.74	683.90	4.70	220.00	2.41	1.10	218.10	2.70	0.87
La	16.08	0.05	0.31	15.46	0.40	24.92	0.16	0.64	25.08	0.16	2.23	0.02	0.90	2.28	0.04	2.24
Ce	33.16	0.25	0.75	32.86	0.90	52.85	0.29	0.55	53.12	0.33	6.37	0.05	0.78	6.55	0.09	2.78
Pr	3.77	0.02	0.53	3.69	0.10	6.79	0.05	0.74	6.83	0.04	1.13	0.01	0.88	1.13	0.02	0.09
Nd	14.37	0.07	0.49	14.04	0.20	28.41	0.10	0.35	28.26	0.37	6.21	0.01	0.16	6.39	0.06	2.85
Sm	3.08	0.02	0.65	3.03	0.00	6.54	0.05	0.76	6.55	0.05	2.23	0.01	0.45	2.27	0.02	1.59
Eu	0.91	0.01	1.10	0.89	0.00	1.97	0.02	1.02	1.99	0.02	0.83	0.01	1.20	0.84	0.01	0.72
Gd	3.04	0.04	1.32	3.01	0.10	6.70	0.08	1.19	6.81	0.08	3.19	0.03	0.94	3.12	0.05	2.15
Tb	0.49	0.01	2.04	0.48	0.00	1.06	0.01	0.94	1.08	0.03	0.58	0.01	1.72	0.59	0.01	1.07
Dy	2.93	0.03	1.02	2.85	0.10	6.36	0.05	0.79	6.42	0.06	3.87	0.03	0.78	3.87	0.06	0.05
Ho	0.60	0.00	0.00	0.59	0.00	1.30	0.01	0.77	1.31	0.01	0.86	0.00	0.00	0.86	0.02	0.35
Er	1.72	0.02	1.16	1.68	0.00	3.62	0.05	1.38	3.67	0.04	2.51	0.03	1.20	2.54	0.04	1.06
Tm	0.26	0.00	0.00	0.25	0.00	0.53	0.01	1.89	0.53	0.01	0.38	0.01	2.63	0.39	0.01	3.31
Yb	1.68	0.02	1.19	1.65	0.00	3.39	0.04	1.18	3.39	0.04	2.52	0.01	0.40	2.53	0.03	0.36

	JA-2 (Imai et al., 1995), n=6					BCR-2 (Wilson., 1997), n=4					JB-2 (GeoREM), n=3					
	Mean	**Std.Dev**	**%RSD**	**Ref.**	**Uncert.**	**Mean**	**Std.Dev**	**%RSD**	**Ref.**	**Uncert.**	**Mean**	**Std.Dev**	**%RSD**	**Ref.**	**Uncert.**	**Accuracy %**
Lu	0.26	0.00	0.00	0.25	0.00	0.51	0.00	0.00	0.50	0.01	0.39	0.00	0.00	0.39	0.01	0.15
Hf	2.97	0.01	0.34	2.84	0.10	4.92	0.03	0.61	4.97	0.03	1.47	0.01	0.68	1.49	0.03	1.14
Ta	0.70	0.04	5.71	0.65	0.00	0.83	0.07	8.43	0.79	0.02	0.04	0.00	0.00	0.04	0.00	1.01
Pb	19.97	0.46	2.30	18.88	0.30	10.32	0.35	3.39	10.59	0.17	4.96	0.09	1.81	5.25	0.11	5.52
Th	4.92	0.07	1.42	4.80	0.10	5.81	0.12	2.07	5.83	0.05	0.26	0.02	7.69	0.26	0.00	0.93
U	2.28	0.04	1.75	2.18	0.10	1.67	0.04	2.40	1.68	0.02	0.15	0.00	0.00	0.15	0.00	1.83

Extended Data Table 3: Trace element averages of certified international reference materials summarised in [74]. Number of runs (n) for each reference material are shown.

End Member	Afar Plume	Depleted Mantle	Pan African Lithosphere	HiMU	EMI	EMII
$^{206}Pb/^{204}Pb$	19.5	17.5	17.85	22	17.4	19.3
$^{207}Pb/^{204}Pb$	15.6	15.3	15.75	15.84	15.48	15.64
$^{208}Pb/^{204}Pb$	39.2	36.6	39.75	40.75	39.0	39.75
$^{87}Sr/^{86}Sr$	0.512875	0.51335	0.5121	0.51285	0.51235	0.51235
$^{143}Nd/^{144}Nd$	0.7035	0.7022	0.7075	0.7025	0.7055	0.709
References	[24, 47]	[24,47]	[24, 47]	[75]	[75]	[75]

Extended Data Table 4: End member compositions used in the principal component analysis.

End Member	PC1	PC2	PC3
$^{206}Pb/^{204}Pb$	0.3714	-0.5488	0.4249
$^{207}Pb/^{204}Pb$	0.5619	-0.1131	-0.5855
$^{208}Pb/^{204}Pb$	0.5727	-0.1835	0.1812
$^{87}Sr/^{86}Sr$	-0.3687	-0.5481	0.2860
$^{143}Nd/^{144}Nd$	0.2872	0.5933	0.6017
Variance explained (%)	53.15	37.42	5.01

Extended Data Table 5: Eigenvectors for the principal components 1-3 when principal component analysis is performed using 5 radiogenic isotope variables. The amount of variance explained by each of the principal components is also included.

References

[70] Stracke, A., Hofmann, A. W., & Hart, S. R. (2005). FOZO, HIMU, and the rest of the mantle zoo. Geochemistry, geophysics, geosystems, 6(5). https://doi.org/10.1029/2004GC000824

[71] McDonough, W. F., & Sun, S. S. (1995). The composition of the Earth. Chemical geology, 120(3-4), 223-253. https://doi.org/10.1016/0009-2541(94)00140-4

[72] Zindler, A., & Hart, S. (1986). Chemical geodynamics. IN: Annual review of earth and planetary sciences. Volume 14 (A87-13190 03-46). Palo Alto, CA, Annual Reviews, Inc., 1986, p. 493-571., 14, 493-571. https://doi.org/10.1146/annurev.ea.14.050186.002425

[73] Rollinson, H. R., Rollinson, H., & Pease, V. (2021). Using geochemical data: to understand geological processes. Cambridge University Press. https://doi.org/10.1017/9781108777834

[74] Jochum, K. P., Willbold, M., Raczek, I., Stoll, B., & Herwig, K. (2005). Chemical Characterisation of the USGS Reference Glasses GSA-1G, GSC-1G, GSD-1G, GSE-1G, BCR-2G, BHVO-2G and BIR-1G Using EPMA, ID-TIMS, ID-ICP-MS and LA-ICP-MS. Geostandards and Geoanalytical Research, 29(3), 285-302. https://doi.org/10.1111/j.1751-908X.2005.tb00901.x

[75] Hart, S. R. (1988). Heterogeneous mantle domains: signatures, genesis and mixing chronologies. Earth and Planetary Science Letters, 90(3), 273-296. https://doi.org/10.1016/0012-821X(88)90131-8